FY21 National Laser Users' Facility Program

M. S. Wei

Laboratory for Laser Energetics, University of Rochester

FY21 was the second year of a two-year period of performance for the 21 National Laser Users' Facility (NLUF) projects (Table I) including ten Academic and Industrial Basic Science (AIBS) experiments approved for the FY20–FY21 shot allocation at the Omega Laser Facility. In total, 360 target shots were taken for 17 NLUF projects during FY21. These NLUF experiments conducted at the facility during FY21 are summarized in this section.

Table I: Twenty-one NLUF (in blue) and AIBS (in gray) projects approved for the FY20–FY21 Omega Laser Facility shot allocations.

Principal Investigator	Institution	Title
F. N. Beg*	University of California, San Diego	Charged-Particle Transport and Energy Deposition in Warm Dense Matter With and Without an External Magnetic Field
C. M. Krauland	General Atomics	Characterization of the Nonlinear Laser–Plasma Interaction in Electron-Assisted Shock Ignition
K. Krushelnick*	University of Michigan	The Dynamics of Strong Magnetic Fields Generated by Relativistic Laser–Plasma Interactions Using OMEGA EP
E. Liang*	Rice University	Collision of Two Magnetized Jets Created by Hollow Ring Lasers
R. C. Mancini*	University of Nevada, Reno	A Laboratory Photoionized Plasma Experiment on OMEGA EP
C. McGuffey*	University of California, San Diego	Driving Compressed Magnetic Fields to Exceed 10 kT in Cylindrical Implosions on OMEGA
R. D. Petrasso*	Massachusetts Institute of Technology	High-Energy-Density Physics, Laboratory Astrophysics, and Student Training on OMEGA
P. Tzeferacos/D. Lamb*	University of Chicago	Fundamental Astrophysical Processes in Radiative Supersonic Magnetohydrodynamic Turbulence
M. Valdivia*	Johns Hopkins University	Demonstration of Monochromatic Talbot–Lau X-Ray Deflectometry Electron Density Diagnostic in Laser–Target Interactions
J. Wicks	Johns Hopkins University	High Pressure and Temperature Polymorphism of a Key Super-Earth Mantle Material: MgO
L. Willingale*	University of Michigan	Direct Laser Acceleration of Electrons for Bright, Directional Radiation Sources
M. Cappelli*	Stanford University	Hydrodynamic Versus Kinetic Atomic Mix in Deflagrating Converging Plasmas
T. Duffy*	Princeton University	Phase Transitions in Planetary Materials at Ultrahigh Pressures
W. Fox*	Princeton University	Magnetic Reconnection in High-Energy-Density Plasmas
R. Jeanloz*	University of California, Berkeley	Multi-Compression and Chemical Physics of Planetary Interiors

Table I: Twenty-one NLUF (in blue) and AIBS (in gray) projects approved for the FY20–FY21 Omega Laser Facility shot allocations (continued).

Principal Investigator	Institution	Title
H. Ji*	Princeton University	Study of Particle Acceleration from Magnetically Driven Collisionless Reconnection at Low Plasma Beta Using Laser-Powered Capacitor Coils
C. C. Kuranz*	University of Michigan	Experimental Astrophysics on the OMEGA Laser
M. J.-E. Manuel	General Atomics	B-Field Effects on Laser–Plasma Instabilities
D. Schaeffer*	Princeton University	Particle Heating by Collisionless Shocks in Magnetized High-Energy-Density Plasmas
B. Srinivasan	Virginia Tech	Investigation of Feasibility of the 11B(P,3α) Reaction in Inertial Confinement Fusion Settings
W. Theobald	University of Rochester	Quantifying Turbulent Rayleigh–Taylor Mixing with X-Ray Phase-Contrast Imaging

*PI's project conducted shots at the Omega Laser Facility in FY21.

Developing Krypton L-Shell Spectroscopy to Study Ion–Electron Equilibration High-Energy-Density Plasmas on OMEGA (ieRate-21A)

Principal Investigators: P. J. Adrian, N. V. Kabadi, C. K. Li, F. H. Séguin, R. D. Petrasso, and J. A. Frenje (Plasma Fusion Science Center, MIT); E. Gallardo-Diaz and R. C. Mancini (University of Nevada, Reno); R. Florido (Universidad de Las Palmas de Gran Canaria); and V. Yu. Glebov, S. P. Regan, and A. Sorce (LLE)

MIT graduate student P. J. Adrian and collaborators led an NLUF experiment to study the physics of ion–electron equilibration in high-energy-density plasmas (HEDP's). The experiments conducted involved the implosion of thin-glass capsules filled with D^3He gas and a trace amount of krypton on the OMEGA Laser System. The implosions produce high density and temperature conditions at peak compression for ion–electron equilibration studies. The primary goal of this study was to develop a new diagnostic technique for determining the electron density (n_e) and electron temperature (T_e) at peak compression through krypton L-shell spectroscopy. The multilayer monochromatic imager (MMI)[1] diagnostic was utilized to measure krypton L-shell lines resolved in time and space. Unfortunately, on this day severe complications with the framing camera used by the MMI prevented the acquisition of critical data of spatially resolved krypton L-shell emission measurements. Time-resolved x-ray spectroscopy data were measured, however, and are shown in Fig. 1. Analysis of the data is still ongoing and will be used in future publications to detail the utilization of krypton L-shell spectroscopy.

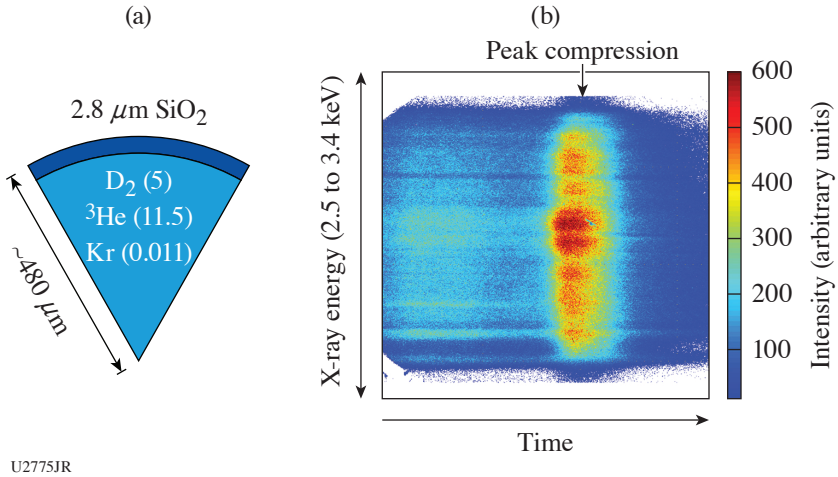

Figure 1
(a) Diagram of the imploded capsule. The gas fills for this experiment were 5 atm of D_2, 11.5 atm of ^3He, and 0.011 atm of krypton. (b) Time-resolved x-ray spectrum in an energy band of 2.5 to 3.4 keV. The x-ray spectrometer clearly resolves x-ray emission at peak compression where the krypton L-shell should be strongly emitting.

This work was supported in part by the National Laser Users' Facility under Contract DE-NA0003938, Laboratory for Laser Energetics under Contract 417532G/UR FAO GR510907. P. J. Adrian was also supported with a DOE SSGF Fellowship under contract DE-NA0003960.

Developing Krypton L-Shell Spectroscopy to Study Ion–Electron Equilibration High-Energy-Density Plasmas on OMEGA (ieRate-21A2)

Principal Investigators: P. J. Adrian, N. V. Kabadi, C. K. Li, F. H. Séguin, R. D. Petrasso, and J. A. Frenje (Plasma Fusion Science Center, MIT); E. Gallardo-Diaz and R. C. Mancini (University of Nevada, Reno); R. Florido (Universidad de Las Palmas de Gran Canaria); and V. Yu. Glebov, S. P. Regan, and A. Sorce (LLE)

Measurements of ion–electron equilibration in the high-density (>10^{23}-cm^{-3}) and high-temperature (>1-keV) regime are necessary to constrain theories on ion–electron transport. This work continues experimental measurements of ion–electron equilibration in this regime. The goal of these experiments was to acquire krypton L-shell emission data from an implosion to determine the electron density (n_e) and electron temperature (T_e) during peak compression. This measurement is critical for determining the plasma conditions achieved in the implosion for the study of ion–electron equilibration. Previous experiments attempting this measurement indicated the krypton L-shell signal to background needed to be increased. To increase the signal, the gas fill of krypton was increased to 0.014 atm, as shown in Fig. 2(a), from previous studies that used 0.011 atm. In addition, a significant background source was x rays from thermal bremsstrahlung emission of the corona. On this day the laser pulse was optimized so that the coronal x-ray emission did not contribute to the x-ray signal during peak compression. The x-ray emission history was measured with a prototype x-ray emission history diagnostic[2] shown in [Fig. 2(b)]. The data clearly indicate that x-ray emission from peak compression is separated from the coronal emission, which decays after the laser turns off. The MMI[3] diagnostic was utilized to measure krypton L-shell lines resolved space at peak compression. Figure 2(c) displays images of the implosion recorded with MMI at peak compression. The data are still under analysis and will be used to diagnose the plasma conditions during peak compression of the implosion, which is critical for studying ion–electron equilibration. Presentations about these experiments are being given at the APS Division of Plasma Physics meeting in 2021.

This work was supported in part by the National Laser Users' Facility under Contract DE-NA0003938, Laboratory for Laser Energetics under Contract 417532G/UR FAO GR510907. P. J. Adrian was also supported with a DOE Stewardship Science Graduate Fellowship (SSGF)under contract DE-NA0003960.

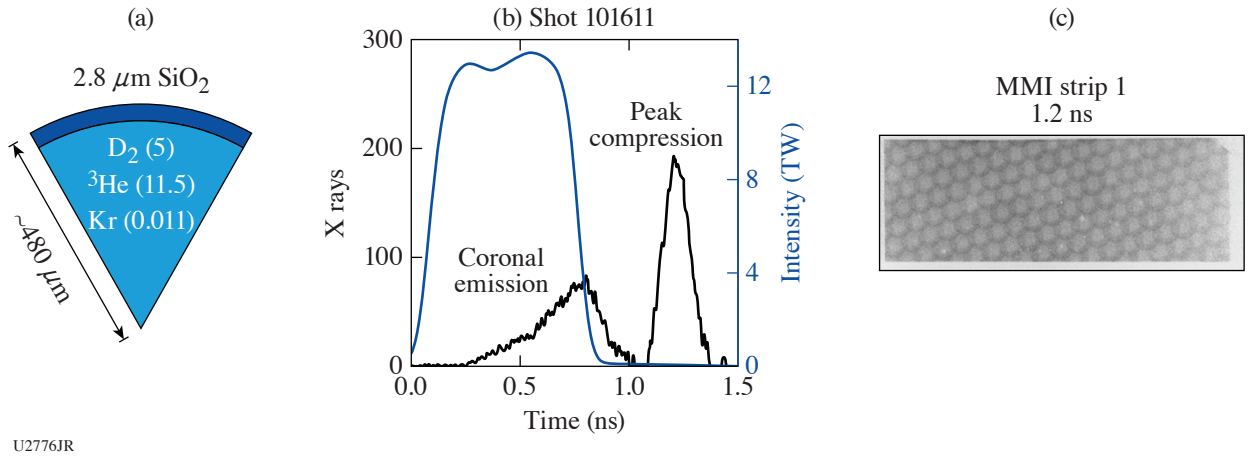

Figure 2
(a) Diagram of the imploded capsule. The gas fills for this experiment were 5 atm of D_2, 11.5 atm of ^{3}He, and 0.014 atm of krypton. (b) Measurement of x-ray emission history relative to the laser pulse. (c) Example MMI data taken during peak compression around 1.2 ns. Data from shot 101611.

Energy Deposition in Magnetized Dense Plasma by Laser-Driven Relativistic Electrons

Principal Investigators: M. Bailly-Grandvaux, K. Matsuo, J. Kim, D. Kawahito, and F. N. Beg (Center for Energy Research, University of California, San Diego); C. McGuffey (General Atomics); J. L. Peebles, J. R. Davies, M. S. Wei, and S. Muller Fess (LLE); P. Gourdain (Department of Physics and Astronomy, University of Rochester), J. Honrubia (Universidad Politécnica de Madrid, Spain); and J. J. Santos (CELIA, University of Bordeaux, France)

Understanding the role of the magnetic field is important for advanced fusion schemes such as fast-ignition inertial confinement fusion and magnetized liner inertial fusion. Here, we report on energy deposition in dense matter by intense laser-driven relativistic electrons with and without an external magnetic field. Thirty-six UV beams with a total energy of ~13.5 kJ are delivered in 1.5 ns to compress a 100-mg/cm^3 CH foam cylinder doped with 1 at. % of Ti. On joint shots, the OMEGA EP beam is injected along the cylinder axis near stagnation time, delivering ~840 J in 10 ps. The magneto-inertial fusion electrical discharge system (MIFEDS) pulsed-power coil provides an external magnetic field of ~18 T at the cylinder target position, which reaches ~1 kT at maximum compression.

In the previous experiment in FY20, the idea was to record, on the same x-ray spectral range (no crystal swap required), both the Ti-dopant emission from the imploded foam and the K-shell emission from fast electrons knocking the two Fe/Cr foils attached on each cylinder end. However, the streaked x-ray spectrometer (SXS) and the time-integrated x-ray spectrometer (XRS) experienced significant background issues when OMEGA EP was fired due to the high noise generated by relativistic electrons. Nevertheless, referring to last year's report, we obtained high-quality measurements of the implosion trajectories and stagnation conditions from the x-ray framing camera (XRFC) and the XRS diagnostic in implosion-only shots. The shots were also highly reproducible, allowing us to benchmark our radiation-hydrodynamic simulations with 2-D *FLASH* and successfully compare implosion trajectories with XRFC results and compressed core conditions with XRS, respectively [see Figs. 3(a) and 3(b)].

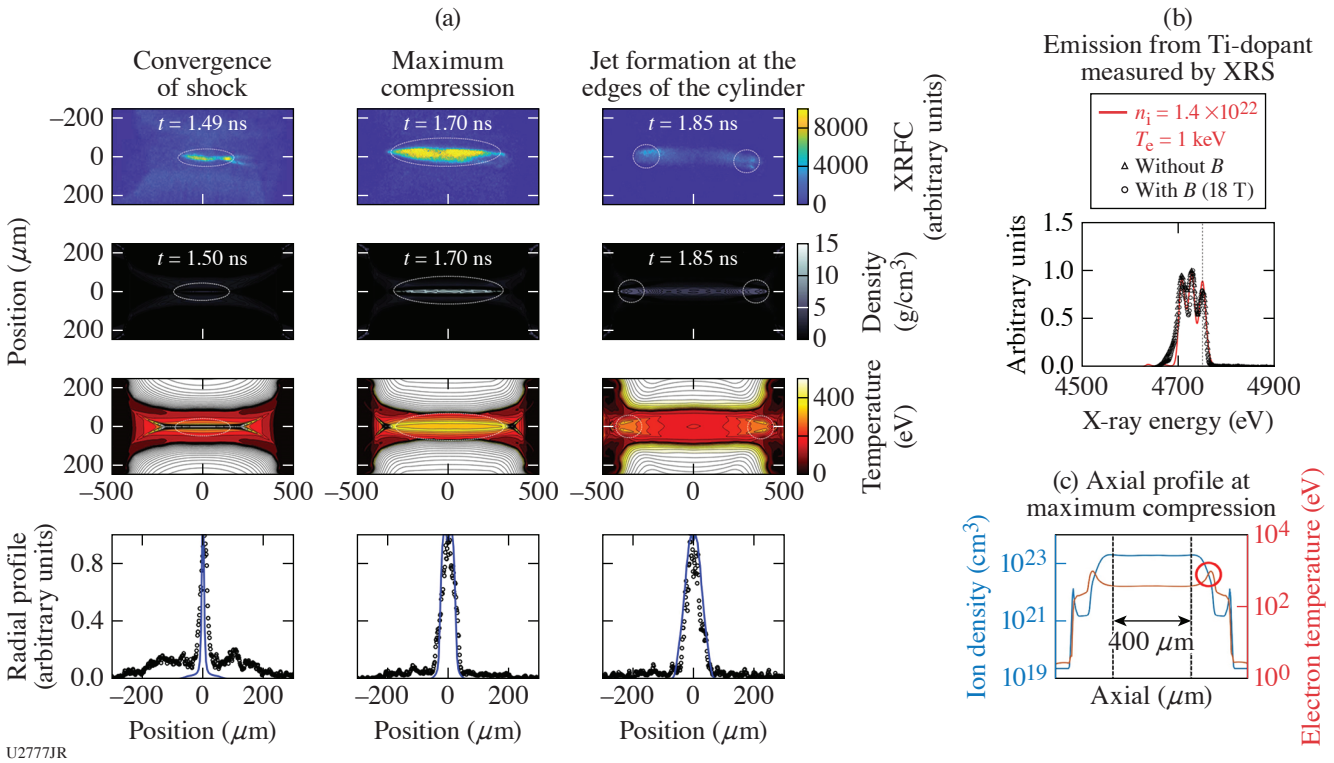

Figure 3

(a) XRFC result (applied B = 18 T) compared with 2-D *FLASH*. (b) XRS titanium-dopant K-shell spectra for B = 0 T and applied B = 18 T, compared to (c) *FLYCK* calculations using the density and temperature extracted from *FLASH* at the edge of the compressed core.

Note that the x-ray emission from the Ti dopant cannot escape from the inside of the compressed core due to opacity effects. Given that the XRS line of sight was along the cylinder's axis, the emission from the edge of the compressed core is the highest contribution to the measured spectra. This hypothesis is validated by the very good agreement between the experimental spectra and the core edge conditions extracted from *FLASH* [Fig. 3(c)].

In the RelEPlasma-21A experiment, we used higher-Z foils (Zn/Cu) attached to each end of the cylinder and fielded the radiation-hardened zinc von Hamos (ZVH) spectrometer tuned to Zn/Cu K-shell emission. The experimental setup and target description are given in Figs. 4(a) and 4(b), respectively. Despite the very high background associated with the joint shots, we successfully recorded Zn and Cu K-shell emission for $B_0 = 0$ T and $B_0 = 18$ T [Fig. 4(d)]. The OMEGA EP beam is injected at $t = 1.65$ ns, which is near maximum compression. We observe an increase of the Zn K_α/Cu K_α ratio for the magnetized shot, which indicates that fewer electrons reached the exit (Cu) side of the cylinder.

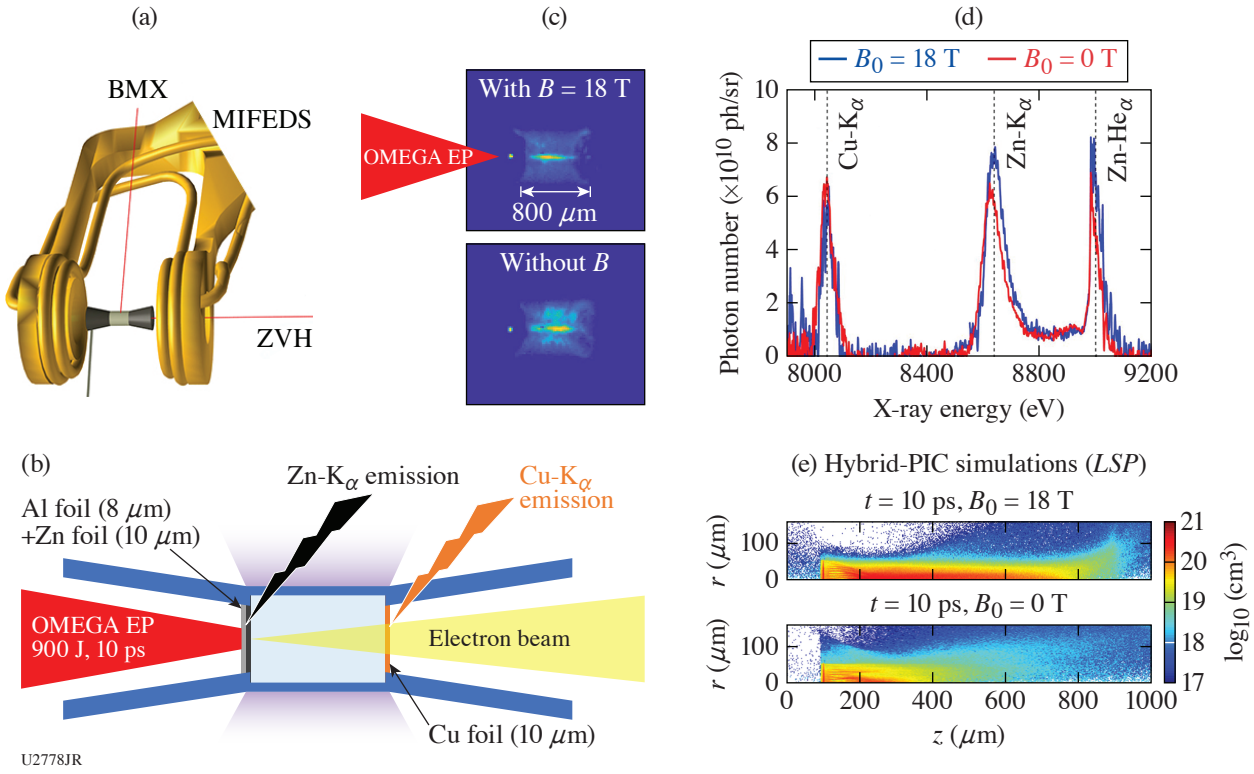

Figure 4
(a) Sketch of the RelEPlasma-21A experimental setup, using the time-integrated ZVH spectrometer, that is shielded against background radiation. (b) Description of the cylinder target for electron transport measurements. (c) X-ray pinhole camera results for joint shots with and without applied B field (18 T). (d) Zn and Cu K-shell emission recorded by the ZVH spectrometer on joint shots. (e) Hybrid-PIC simulations of the electron transport in the compressed cylinder, with and without applied B field. The hybrid-PIC simulations use maps of the plasma density and temperature extracted from *FLASH* near maximum compression ($t = 1.65$ ns).

To unravel the electron transport behavior with and without an applied B field, we carried out 2-D hybrid-PIC (particle-in-cell) simulations using the *LSP* code. The OMEGA EP electron source was previously characterized using full-PIC simulations and compared with results from an electron spectrometer.[4] We imported the maps of hydrodynamic plasma quantities from the 2-D *FLASH* simulations for $t = 1.65$ ns. The *FLASH* simulations were performed for both $B_0 = 0$ T and $B_0 = 18$ T, including the magnetohydrodynamic (MHD) packages in *FLASH* to compute the compressed B field. The background resistivity of the CH at various temperature (and densities) called for the use of advanced resistivity models in *LSP*. As discussed in Ref. 4, the compressed magnetic field of ~1 kT is strong enough to guide ~5-MeV electrons in the compressed core of ~15-μm radius. Consequently, the fast electrons can propagate deeper into the compressed core when the cylinder is magnetized, enabling more

efficient energy deposition via collisions with the dense compressed core. On the other hand, in the unmagnetized cylinder, the fast electrons are mirrored or scattered near the compressed core edges and reach the rear side primarily through the low-density outer part of the cylinder (at higher radii), therefore without experiencing a strong drag. This can be qualitatively observed in the x-ray pinhole camera images shown in Fig. 3(c), where more emission is seen outside the core versus inside the core for the unmagnetized shot versus the magnetized shot. Overall, the number of electrons reaching the rear side of the cylinder will be reduced in the magnetized case due to the enhanced energy deposition. Figure 3(e) shows snapshots of the fast-electron density for the unmagnetized and magnetized cases. The above-described fast-electron-transport behavior between magnetized and unmagnetized targets is clearly observed in simulations.

The remaining analysis involves calculating the synthetic time-integrated K_α emission from the Zn and the Cu channel using the fast-electron macroparticle information from the hybrid-PIC simulations. It requires consideration of the bulk temperature, density, and kinetic energy dependence of the K_α cross sections, as well as optical depth effects of the Zn emission radiation transport through the compressed cylinder.

This work was supported by the National Nuclear Security Administration through the National Laser Users' Facility Program NA0003943.

Deposition of Intense Proton Beams in Cu and Resultant Heating

Principal Investigators: M. Bailly-Grandvaux, K. Bhutwala, and F. N. Beg (Center for Energy Research, University of California, San Diego); C. McGuffey (General Atomics); D. Mariscal and T. Ma (LLNL); and P. M. Nilson and W. Theobald (LLE)

The OMEGA EP short-pulse laser can deliver proton and ion beams with tens of joules that can then deposit their energy in bulk samples, leading to rapid, uniform heating. ProtonWDM-EP-21A is the second shot day of a pair of NLUF shot days studying energy deposition of proton beams in solid matter. On the first shot day in FY20, a thin Si wafer was heated by protons and probed by x-ray absorption spectroscopy using a short-pulse–driven continuum backlighter. It was observed that Si K-shell absorption evolved from a single K-edge feature to a blurred K edge to a sequence of up to a dozen absorption features within a matter of 100 ps (Ref. 5) In the upcoming shot day, protons will be focused into Cu disks (10 or 25 μm thick × 200 μm diameter), and x-ray emission diagnostics will observe the heating of the disk, which is expected to reach $\gg$100 eV through proton then ion heating. The samples are much thicker than the thin Si foils used in FY20. The thicker samples will produce sufficient emission for line spectroscopy and imaging; however, they are still expected to be heated uniformly in depth with minimal self-absorption. Proton beam transport in an even-thicker material (plastic foam) has also been studied by this group using OMEGA EP.[6]

Unlike in ProtonWDM-EP-20A and pIsoHeat, a steep-walled hollow cone will be attached to the rear of the target foil and the front of the Cu sample. Such a cone has been shown to funnel the proton beam into a small spot.[7] The cone has a 100-μm opening at the tip. The target and diagnostic lines of sight for these shots are shown in Figs. 5(a) and 5(b). Another type of shot is planned for the shot day in which the proton beam will be incident, without strong focusing in this case, onto a bulk Cu slab. The slab will catch only half of the beam, and radiochromic film will measure the unblocked and transmitted portions. This will be this group's first attempt to measure energy deposition of the OMEGA EP-driven proton beam with absorption directly in the intense beam on a single shot. This configuration is shown in Fig. 5(c). New hardware for the radiochromic film, developed through the Omega Laser Facility Users Group (OLUG) recommendations process, will be fielded on this shot day.

This work was supported by the National Nuclear Security Administration through the National Laser Users' Facility Program NA0003943.

Cylindrical Compressions with Embedded B Fields to Characterize Strongly Magnetized Hot Dense Plasmas

Principal Investigators: M. Bailly-Grandvaux and F. N. Beg (Center for Energy Research, University of California, San Diego); R. Florido (University of Las Palmas de Gran Canaria, Spain); G. Perez-Callejo, J. J. Santos, and C. Vlachos (CELIA, University of Bordeaux, France); C. A. Walsh (LLNL); F. Suzuki-Vidal (Imperial College, UK); C. McGuffey (General Atomics); R. C. Mancini (University of Nevada, Reno); M. A. Gigosos (Universidad of Valladolid, Spain); and J. L. Peebles, J. R. Davies, and S. Muller-Fess (LLE)

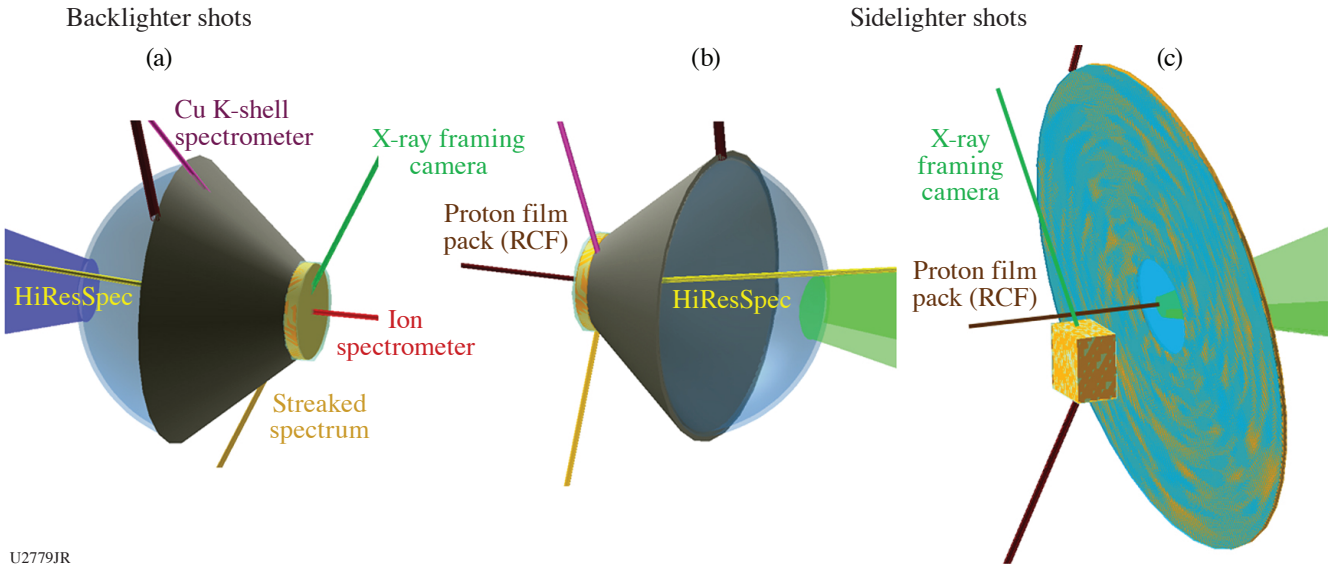

Figure 5
[(a),(b)] Experimental configurations for the Cu disk heating experiment and (c) the proton energy deposition measurement. The first two configurations will use the same laser and target conditions but have complementary diagnostics. Configuration (c) will provide a simple measurement of energy deposition as well as time-resolved images of the top Cu face, giving a cross-sectional view of the emission profile.

The use of external magnetic fields in inertial confinement fusion (ICF) has been identified as a promising way to assist ignition. In this relatively new area of research, the magnetic-field transport during compression and related magnetized plasma dynamics must be studied. We proposed a platform for the OMEGA laser to study MHD effects in cylindrical implosions at regimes of large magnetic pressure and magnetization. Cylindrical targets were filled with Ar-doped D_2 gas and symmetrically imploded using a 40-beam, 14.5-kJ, 1.5-ns laser drive. To investigate the effects of magnetization, implosions were characterized using x-ray imaging and Ar K-shell line-emission spectroscopy. Two-dimensional simulations using the MHD code *GORGON* predicted that a seed B field of 30 T should be compressed to ~30 kT. As a result, the characteristic conditions of the compressed core and the emitted Ar spectrum are expected to be modified.[8] We performed implosions with a seed B-field induced from (or using) laser-driven coils [Fig. 6(a)] and MIFEDS [Fig. 7(a)]. According to proton probing results, the B-field generated seed with laser-driven coils was <6 T [Fig. 6(b)] during the BCoilCompress-20A shot day, likely due to the large inductance of the coils. This seed B field was too low to affect the core conditions [Fig. 6(c)]. A dual-MIFEDS design provided a seed B field of ~25 T in the recent BCoilCompress-21A shot day; the result was observation of systematic changes in the Ar spectra between unmagnetized and magnetized shots [Fig. 7(c)]. Carrying out such magnetized implosion experiments will advance the modeling of B-field compression and diffusion along with the benchmarking of atomic kinetics and line shape calculations in magnetized plasmas relevant to complex ICF-related experiments with embedded B fields.

In the latest BCoilCompress-21A Campaign, eight target shots were taken, including two pointing shots at the beginning of the shot day. Four shots were magnetized with a seed B field of ~25 T and two were unmagnetized, i.e., MIFEDS was not charged. In Fig. 7(b), we present a typical x-ray framing camera result. Before 1.3 ns, we can see solely the emission from the plastic shell moving inward at a velocity evaluated around ~230 km/s. After 1.3 to 1.4 ns, the core is being assembled along the central axis, with a peak emission (~max compression) occurring around 1.5 to 1.6 ns. Those numbers are in line with previous cylindrical implosion data from the SmallMagLIF Campaigns, noting that our shell thicknesses were between 18 and 20 μm during our FY21 shot day. In addition, measurements from the fixed, gated x-ray imager diagnostic found a compressed core radius of 12 to 15 μm, which corresponds to a convergence ratio (CR) of ~20. This is ~30% of what simulations predict: a similar observation as in Ref. 9. Accordingly, assuming mass conservation, the compressed core density is ~1 g/cm^3, in agreement with the inferred electron density from the Ar K-shell spectra of the XRS time- and space-integrated spectrometer.

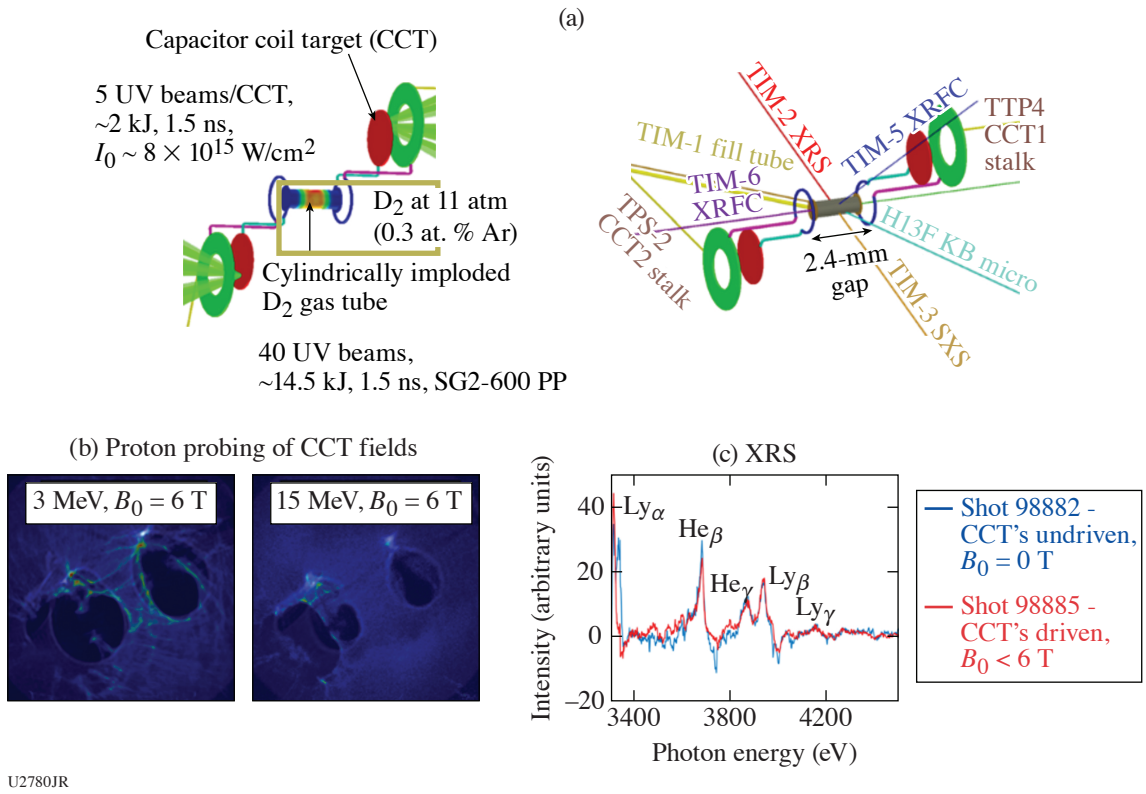

Figure 6
(a) Experimental setup of the BCoilCompress-20A shot day, using laser-driven capacitor coil targets (CCT's) to generate the seed B field. (b) Overlay of experimental and synthetic (for B_0 = 6 T) proton deflectometry images, showing some current asymmetry in the coils and matching prediction for B_0 < 6 T. (c) Ar x-ray line emission for undriven (blue) and driven (red) CCT's.

Despite the lower convergence ratio than in simulations and shell thickness variations of the order of ±1 μm across our target batch, a high reproducibility of the Ar spectra recorded with XRS was observed for each of the two distinct scenarios, unmagnetized or magnetized. More interestingly, regardless of the small differences in the target shell thickness, several systematic observations are seen in the time-integrated Ar spectra [Fig. 7(c)]. For the magnetized shots, the following line-intensity ratios are higher: (a) Ly$_\beta$/He$_\beta$, (b) Ly$_\alpha$/He-like satellites, and (c) He$_\alpha$/Li-like satellites, therefore suggesting a higher electron temperature for the magnetized implosion core. These observations are consistent with the impact of the compressed B field on the core conditions and have been predicted, at least in a qualitative manner, by our synthetic spectra simulations. Finally, note that the Ar line emission is dominated by the core conditions, as seen in the time-resolved spectra of Fig. 7(d). This indicates that there is no impact in the XRS data from Ar contamination in the shell nor is there evidence of a premature breakup of the shell.

We also observed a systematic increase of the neutron yield and neutron-inferred ion temperatures when adding the B field. The shot-to-shot variability of neutron diagnostics is higher, however, than what we observed from the Ar spectra in the same conditions. It points toward the use of x-ray emission diagnostics with a dopant in the gas to extract global trends of a magnetic field (or else) on the core formation and thereby alleviate the large variability associated with neutron measurements. The combination of the two types of measurements is very valuable, particularly considering that, due to opacity effects, the emission spectroscopy results might be more sensitive to the core edge compared to neutron measurements.

More analysis is needed to weigh the effects of nonuniform plasma conditions on the spectroscopy data and to assess the significance of the neutron-inferred quantities at this yield level. In a future experiment, we will focus on optimizing the laser pointing and target alignment, as well as the target quality and variability, to reach higher convergence ratios and thereby lower plasma β.

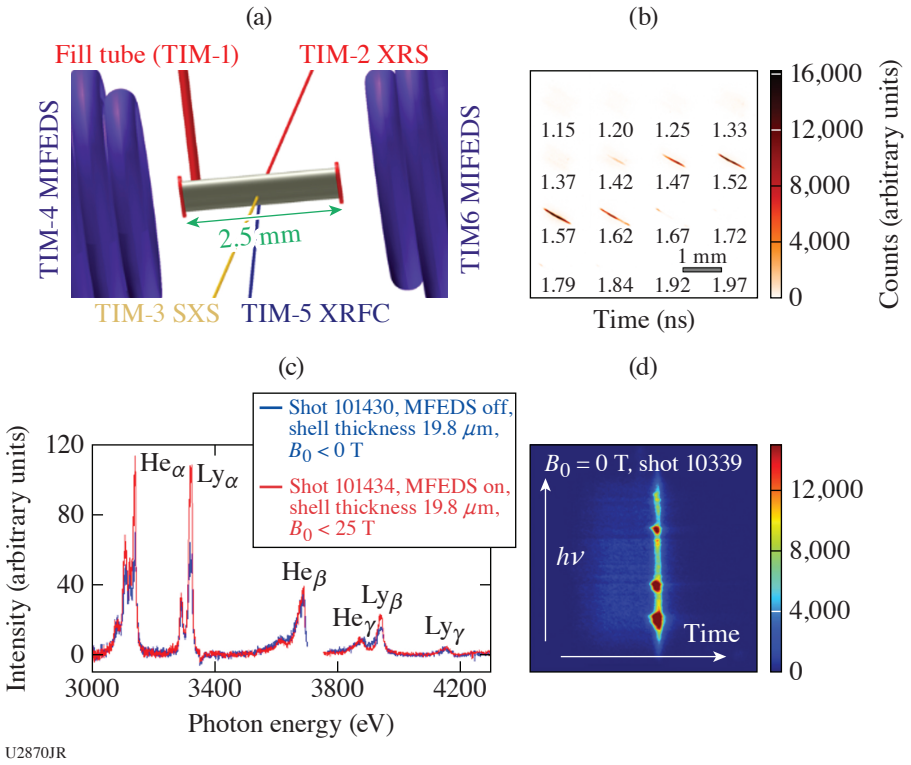

Figure 7
(a) Experimental setup of the BCoilCompress-21A shot day, using dual MIFEDS to generate an ~25-T seed B field. (b) Example result from the XRFC, monitoring the implosion trajectories. (c) Ar x-ray line-emission spectra for a pair of unmagnetized (blue) and magnetized (red) shots; the comparison is consistent with higher T_e with the field. (d) A time-resolved Ar x-ray line-emission spectrum, which shows that the Ar spectra are dominated by the core emission.

The magnetic pressure should have a greater effect on the assembled core density, leading to the rise of specific extended-MHD effects of great interest for magneto-inertial fusion, namely induced currents and nonlocal electron transport (discussed in Ref. 8).

In parallel, we will further pursue our investigation of laser-driven coil designs for OMEGA. Our first experiment confirmed the critical importance of the large coil inductance at the imposed 1.5-ns irradiation duration (which needed to be the same as the implosion drivers). We are exploring designs with lower inductance that would still be compatible with the constraints of cylindrical compressions and could potentially produce B fields higher than MIFEDS.

This work was supported by the NNSA/NLUF Grant DE-NA0003940. M. Bailly-Grandvaux received a new grant (DE-SC0022250) for this project from DOE Office of Science High-Energy-Density Laboratory Plasmas (HEDLP) Program for FY21–FY24.

Studies of Strongly Magnetized Electrons and Ions on Heat Flow and Symmetry in Shock-Driven Implosions
Principal Investigators: J. A. Frenje, C. Chang, N. V. Kabadi, and P. J. Adrian (MIT); J. L. Peebles (LLE); and C. A. Walsh (LLNL)

The MagImp-21 Campaign included two half-day experiments (MagImp-21A and 21B) on OMEGA to study the impact of strongly magnetized electrons and ions on electron thermal transport (and asymmetries in the thermal transport), ion Knudsen number, and ion and electron viscosity. This campaign is a central part of MIT student C. Chang's Ph.D. thesis.

These experiments used thin-glass capsules filled with 90% D_2 and 10% ^{3}He gas driven by a 1-ns square pulse delivering about 16 kJ to the capsule. Since the glass shell was ablated at peak compression in these experiments, the observables are mainly

due to the shock-driven plasma conditions. MIFEDS was used to apply an initial B field to the implosion. A large set of nuclear and x-ray diagnostics was used to measure yield, electron temperature and electron-temperature profiles, implosion trajectory, implosion size, and x-ray emission source profiles in different energy bands. The MagImp-21A experiment conducted at an initial B field of 50 T generated some great data. For example, the nuclear emission history increased by 20% in the magnetized case than in the nonmagnetized reference case. In addition, the electron temperature and electron-temperature profile went up 10% and steepened 3×, respectively. These examples shown in Fig. 8 highlight the results from the MagImp-21A experiment. Detailed data analysis is ongoing, and results will be prepared for publication. In contrast, MagImp-21B, which was to be executed at 20 T, did not occur because of MIFEDS failure just before the first magnetized experiment. The hope is to have the MagImp-21B rescheduled in FY22.

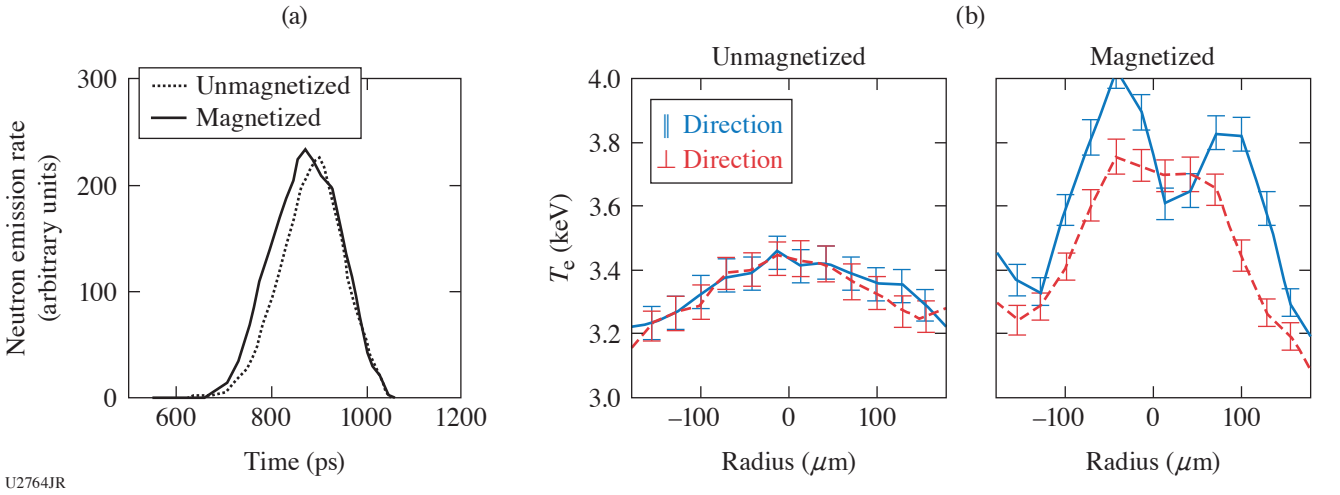

Figure 8
Main results from the MagImp-21A experiments. (a) Nuclear-emission history for the 50-T magnetized case (solid curves) and unmagnetized case (dotted curves). (b) Electron-temperature profiles for the unmagnetized and the 50-T magnetized case. The red and blue curves indicate the electron-temperature profiles in the direction perpendicular and parallel to the magnetic-field lines, respectively.

This work was supported in part by the National Laser Users' Facility under Contract DE-NA0003938, and Laboratory for Laser Energetics under contract 417532G/UR FAO GR510907.

The NuclSyn-21 Campaign for Measurements of the ^{3}He^{3}He Proton Spectrum and Platform Development for CNO Studies
Principal Investigators: M. Gatu Johnson, P. J. Adrian, J. A. Frenje, T. M. Johnson, N. V. Kabadi, J. Kunimune, C. K. Li, J. Pearcy, F. H. Séguin, G. D. Sutcliffe, and R. D. Petrasso (MIT); B. D. Appelbe, A. J. Crilly, and G. Kagan (Imperial College, UK); C.J. Forrest, V. Yu. Glebov, O. M. Mannion, F. J. Marshall, and C. Stoeckl (LLE); L. M. Green, B. M. Haines, B. D. Keenan, and W. T. Taitano (LANL); and H. W. Sio (LLNL)

The NuclSyn-21 Campaign included two half-day OMEGA experiments: (1) N_2D_2 and (2) ^{3}He^{3}He, with the broad joint goal of furthering efforts to study nucleosynthesis-relevant nuclear reactions using the ICF Platform.

The goals of the N_2D_2 experiment were to test the feasibility of using the ICF platform for carbon-nitrogen-oxygen (CNO)-cycle-relevant nuclear studies and also to study shock coupling physics. The shots used thin plastic shell capsules filled alternatively with an N_2D_2 gas mixture or pure D_2 gas to test the impact of adding the heavier N ions on the performance of shock-driven implosions. A large set of nuclear and x-ray diagnostics was brought to bear to study yield, ion temperature (T_i) and electron temperature, implosion size, and x-ray emission. T_i inferred from the DD-n neutron spectrum from the N_2D_2-gas–filled implosions was found to be slightly higher than for the D_2-only implosions. The DD-n yield from the D_2-only implosions was found

to be ~6× higher than the yield from the mix-fill implosion, with a factor of 4 expected based on the difference in deuterium number density only. These results suggest that the shock-driven ICF platform will be feasible for CNO experiments. Detailed data analysis is ongoing, and results will be prepared for publication.

The ^{3}He + ^{3}He → α + p + p reaction is the main energy-producing step in our sun, and the basic nuclear physics governing this reaction are not well understood. An improved understanding of the fusion-product spectrum for this reaction can substantially impact inference of its S-factor from accelerator experiments, which will feed directly into solar models, impact predicted rates of solar neutrinos, and thus constrain modeling of solar dynamics. The goal of the ^{3}He^{3}He experiment was to extend earlier OMEGA experiments where the ^{3}He^{3}He proton spectrum was measured at proton energy $E_p > 6$ MeV [Fig. 9(a)][10] with a measurement of the lower-energy protons at $1.5 < E_p < 6$ MeV. Such data would much better constrain modeling of this reaction [Fig. 9(a)]. Two new diagnostics were brought to bear to make this measurement: a new MagSpec spectrometer [Fig. 9(b)] and an optimized step-range-filter design [Fig. 9(c)].[11] Data analysis is still in progress but initial results look promising, suggesting data were obtained at least down to E_p = 1.5 MeV.

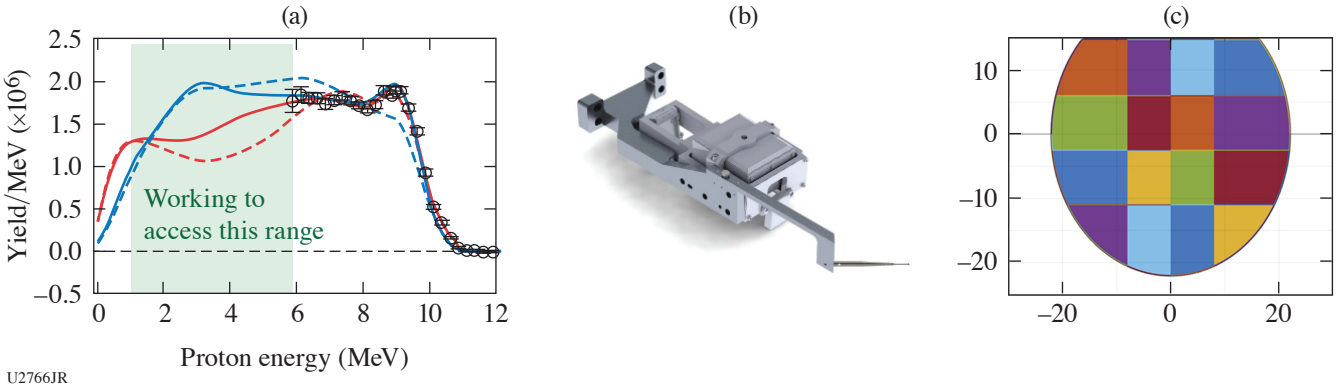

Figure 9
(a) Proton spectrum from the ^{3}He^{3}He reaction previously measured on OMEGA as published in Ref. 10. Until NuclSyn-21, the spectrum was only measured at proton energy $E_p > 6$ MeV. Data below 6 MeV are required to strongly constrain modeling of the reaction, as can be understood from looking at the colored lines that represent different models. The NuclSyn-21 experiments aimed to access the range highlighted in green through the use of two new diagnostic capabilities: (b) MagSpec, which consists of an aperture fielded in a ten-inch manipulator (TIM) at 20 cm from target chamber center (TCC) for high detection efficiency, a bending magnet, and a CR-39 detector, and (c) a new, optimized step-range-filter design, with 16 tantalum filters of various thickness fielded in front of a piece of CR-39 to allow inference of the full broad proton spectrum from ~1.5 to 12 MeV (Ref. 11).

This work was supported in part by the National Laser Users' Facility under Contract DE-NA0003938, Laboratory for Laser Energetics under Contract 417532G/UR FAO GR510907, and Lawrence Livermore National Laboratory under Contract B640112.

Performance Scaling of Inverted-Corona Neutron Sources

Principal Investigator: M. Hohenberger (LLNL)
Co-investigators: N. Meezan and A. J. Mackinnon (LLNL); J. Pearcy and N. V. Kabadi, (Plasma Science and Fusion Center, MIT); W. Riedel and M. Cappelli (Stanford University); S. H. Glenzer (Stanford University); and C. J. Forrest (LLE)

Experiments were performed on the OMEGA laser to study the performance of the inverted-corona neutron platform. Laser beams were incident onto the inside surface of a sphere through laser entrance holes, thereby ablating a layer of fusion fuel, e.g., a CD liner.[12] Fuel may also be provided as a gas fill.[13] In either case, the fuel plasma stagnated on center and was heated to fusion conditions. Such targets have shown promise as neutron sources for high-energy-density applications, and experiments at the National Ignition Facility (NIF) are planned to apply this platform to radiochemistry applications such as neutron cross-section measurements. Previous experiments performed on OMEGA demonstrated a surprising yield dependence on the CD-liner thickness, indicating mix in the ablating plasma. Experiments with D_2-gas–filled, CH-wall targets also indicated mix

of the wall material into the gas fill as a potential limiting factor in the performance. This suggested that the addition of a CD liner to gas-filled targets should mitigate some of the mix-induced yield degradation,[13,14] as was confirmed computationally in PIC simulations modeling the gas–ablator interface.[15]

Targets were 1.8-mm-diam capsules driven by 40 OMEGA beams (1-ns square pulses, ~19 kJ) [see Fig. 10(a)]. The shot day comprised three parts: (1) yield scaling with CD-liner thickness in a vacuum target; (2) D_2-gas–filled targets with a CD liner; and (3) CD-lined targets with a ^{3}He fill to diagnose gas–ablator mix via proton emission from D–^{3}He reactions. The vacuum target performance scaled as expected and was consistent with previous data [Fig. 10(b)],[12,13] although no yield improvements were observed for a CD-liner thickness >2 μm. Adding a CD liner to gas-filled targets increased the yield by ~2× from Y_n ~3.2 × 10^{10} to Y_n ~ 1.5 × 10^{10} compared to a CH-only capsule [Fig. 10(c)]. Finally, no correlation was observed between proton or D–D neutron yield and CD-liner thickness in ^{3}He-filled targets. In contrast to previous data, these results suggest that only the innermost few microns of wall material affect the hot-spot conditions.

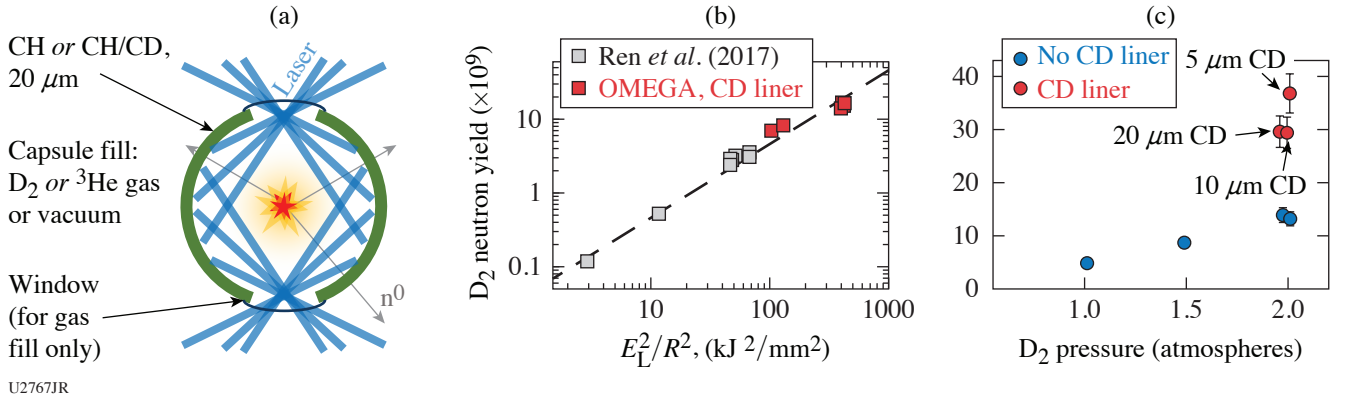

Figure 10
(a) The capsule is laser irradiated on the inside surface via two laser entrance holes. (b) In CD-lined targets, the neutron yield scaled as expected with laser energy and target size. (c) Adding a CD liner significantly increased the neutron yield from D_2-gas-filled targets.

Gas-Jet Collisionless Shock Experiments on OMEGA

Principal Investigators: T. M. Johnson, G. D. Sutcliffe, J. A. Pearcy, A. Birkel, N. V. Kabadi, B. Lahmann, P. J. Adrian, B. L. Riechelt, J. Kunimune, and C. K. Li (Plasma Science and Fusion Center, MIT); H. Chen (LLNL); J. Katz (LLE); and V. T. Tikhonchuk (Université de Bordeaux, Eli Beamlines)

Collisionless shocks are a common phenomena in the universe that are not well understood. They can be found inside our solar system, in supernova remnants, and in active galactic nuclei. When two collisionless plasma sheets collide at high velocity, instabilities redistribute kinetic energy by generating electromagnetic fields. These fields in turn interact with the plasma, forming a shock and dissipating even more energy in field generation, plasma heating, and particle acceleration. Recent pMagShock-21A experiments on the OMEGA laser, which is part of MIT student T. M. Johnson's Ph.D. thesis, successfully created collisionless shocks. In this experiment, lasers drive a CH hemispherical target to launch a supersonic plasma flow (>1500 km/s). This supersonic plasma flow collides with a volume of hydrogen gas provided by the gas-jet system. A schematic drawing of the experiment is shown in Fig. 11(a). The hydrogen gas is ionized by reflected laser light and bremsstrahlung from the plasma flow. When these two plasmas collide, a collisionless shock is formed. We diagnosed this system using imaging 2ω Thomson scattering, D^{3}He backlit proton radiography, and electron spectroscopy [Osaka University electron spectrometer (OU-ESM) and electron–positron–proton soectrometer (EPPS)]. In total, our experiment consisted of 13 shots split between a Thomson-scattering configuration and a proton radiography configuration.

Thomson scattering provided very valuable information about the spatial structure of the collisionless shock. Namely, we observed large increases in density and temperature, as shown in Figs. 11(b) and 11(c), respectively. This gives a measurement of

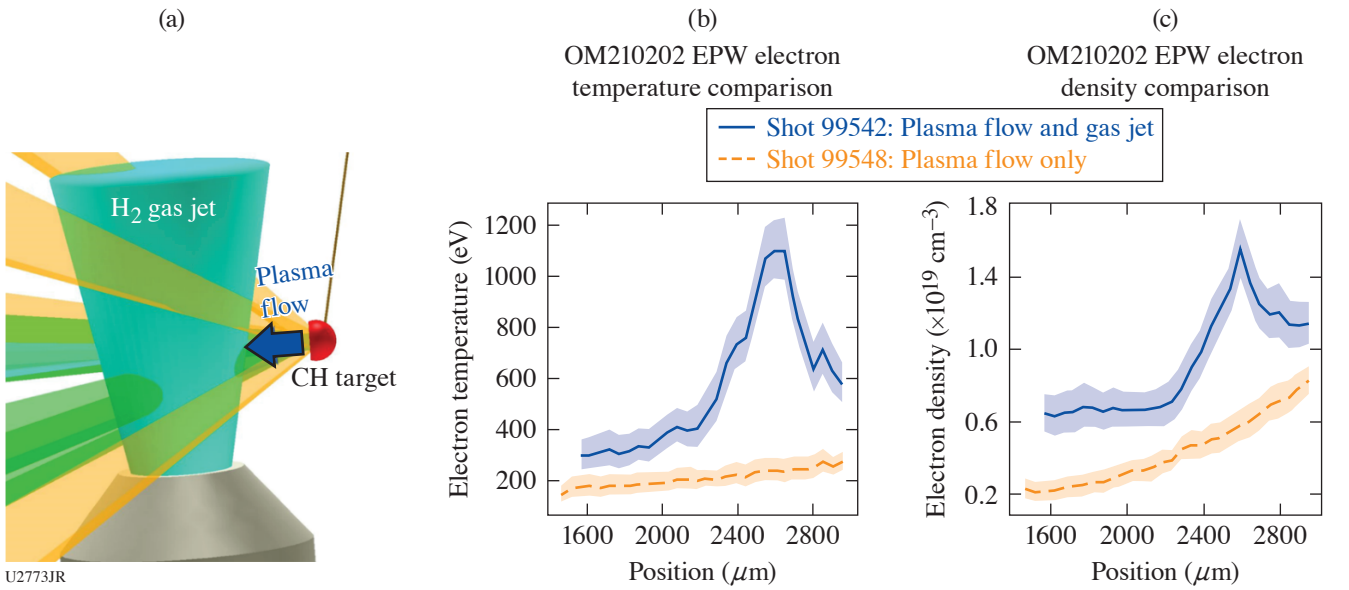

Figure 11
(a) A CAD rendering of the experimental configuration. (b) Imaging Thomson-scattering–measured electron temperature. The comparison is between shots without the gas jet (not interaction) and shots with both the gas jet and plasma flow (with interaction). A large increase in temperature is observed, indicating shock formation. (c) Imaging Thomson-scattering–measured electron density. Similar to the electron temperature, an increase in density is observed. EPW: electron plasma wave.

the size of the shock. The Thomson-scattering data also provided a measurement of the flow velocity, which confirms that our system has very low collisionality. Additionally, proton radiography measurements show a clear shock structure, and electron spectroscopy measurements show that electrons are accelerated into a power-law distribution. Work is ongoing to finalize the analysis of these data and to perform comprehensive MHD and PIC simulations.

This work was supported in part by the National Laser Users' Facility under Contract DE-NA0003938 and Laboratory for Laser Energetics under Contract 417532G/UR FAO GR510907.

Measurement of Multiple Nuclear Emission Histories in the Transition from Shock to Compression-Dominated Implosions
Principal Investigators: N. V. Kabadi, P. J. Adrian, and J. A. Frenje (Plasma Science and Fusion Center, MIT)

The primary goal of these experiments was to collect data related to multi-ion and kinetic effect in the transition from shock-dominated to compression-dominated implosions by varying the shell thickness in glass capsules. It was previously found that ion species separation and thermal decoupling between ion species impact nuclear emission during the shock-convergence and rebound phases.[16] The experiments were designed to determine if these effects impact the subsequent compression phase. The primary data for this investigation are the DD-n yields and ion temperatures from neutron times of flight (nTOF's), D^3He-p yields and spectra from the wedge-range filter spectrometers, and simultaneous measurement of the DD-n and D^3He-p emission histories on the particle x-ray temporal diagnostic (PXTD). The PXTD data collected on shots with a 4-μm-thick shell show a fully shock-dominated emission history as shown in Fig. 12, while data collected with 9.5-μm-thick shells have separate D^3He-p shock and compression components as also shown in Fig. 12. The arrival histories at the scintillator 3 cm from target chamber center (TCC) can also be seen in Fig. 12. These will be corrected for the particles' times of flight pending CR-39 processing. The two emission histories will be determined with ~10-ps cross timing uncertainty. The ratio of the DD-n to D^3He-p emission histories in combination with the total yields and burn-averaged ion temperatures will be used to determine if the data are consistent with average-ion hydrodynamics.

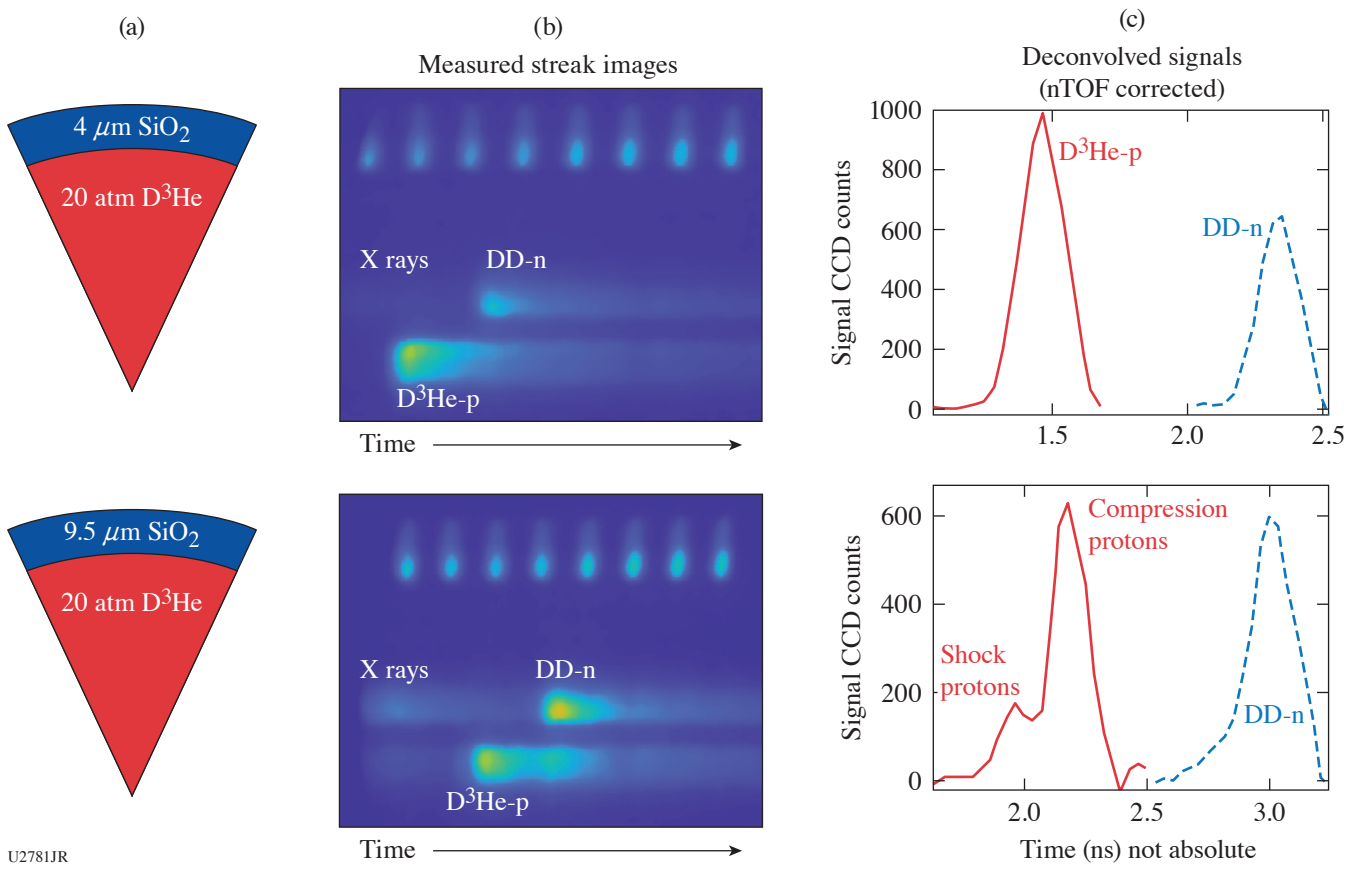

Figure 12
Examples of the PXTD data collected on the OMEGA shot day PXTD-20A, delayed to FY21. Using the PXTD, the DD-n and D3He-p emission histories were captured on a single diagnostic, allowing detailed comparison of their relative timing. The implosion with a 4-μm-thick shell shows D^3He-p and DD-n histories dominated by a shock flash component while the 9-μm-thick shells produced DD-n dominated by compression and D^3He-p with both shock and compression components.

This material is based upon work supported by the Department of Energy, National Nuclear Security Administration under Award Nos. DE-NA0003868 and DE-NA0003938.

Measurement of Multiple Nuclear Emission Histories in Hydro-Equivalent Shock-Driven Implosions
Principal Investigators: N. V. Kabadi, P. J. Adrian, and J. A. Frenje (Plasma Science and Fusion Center, MIT)

The goal of this study is to better understand the previously observed multi-ion dynamics during the shock convergence phase of ICF implosions.[17,18] These experiments used thin glass shells filled with high-density, 3.5-mg/cm^3 gas comprised of mainly deuterium and ^{3}He with a trace amount of tritium. More details of the experimental configurations are shown in Fig. 13. The initial gas density was held constant while varying the D:^{3}He fill ratio, making the implosions hydrodynamically equivalent. The fill ratios allow simultaneous measurement of the DD-n, DT-n, and D^3He-p emission histories with the PXTD.[17] By measuring all three histories on a single diagnostic, they can be compared with ~10-ps relative timing accuracy. An example of this data is shown in Fig. 13. PXTD uses fast-rise scintillators coupled to an optical streak camera so all of the information is encoded in the rising edges. To interpret the PXTD data, the emitted D^3He-p spectrum measured with wedge-range-filter (WRF) spectrometers is also critical; example spectra are included in Fig. 13. From these data, the source of previously observed bang-time separation can be determined. It will be attributed to multi-ion diffusion, kinetics, or hydrodynamics based on how the bang-time separation varies with initial fill ratio. Analysis and preparation for publication are ongoing.

This work was supported in part by the National Laser Users' Facility under Contract DE-NA0003938, Laboratory for Laser Energetics under Contract 417532G/UR FAO GR510907.

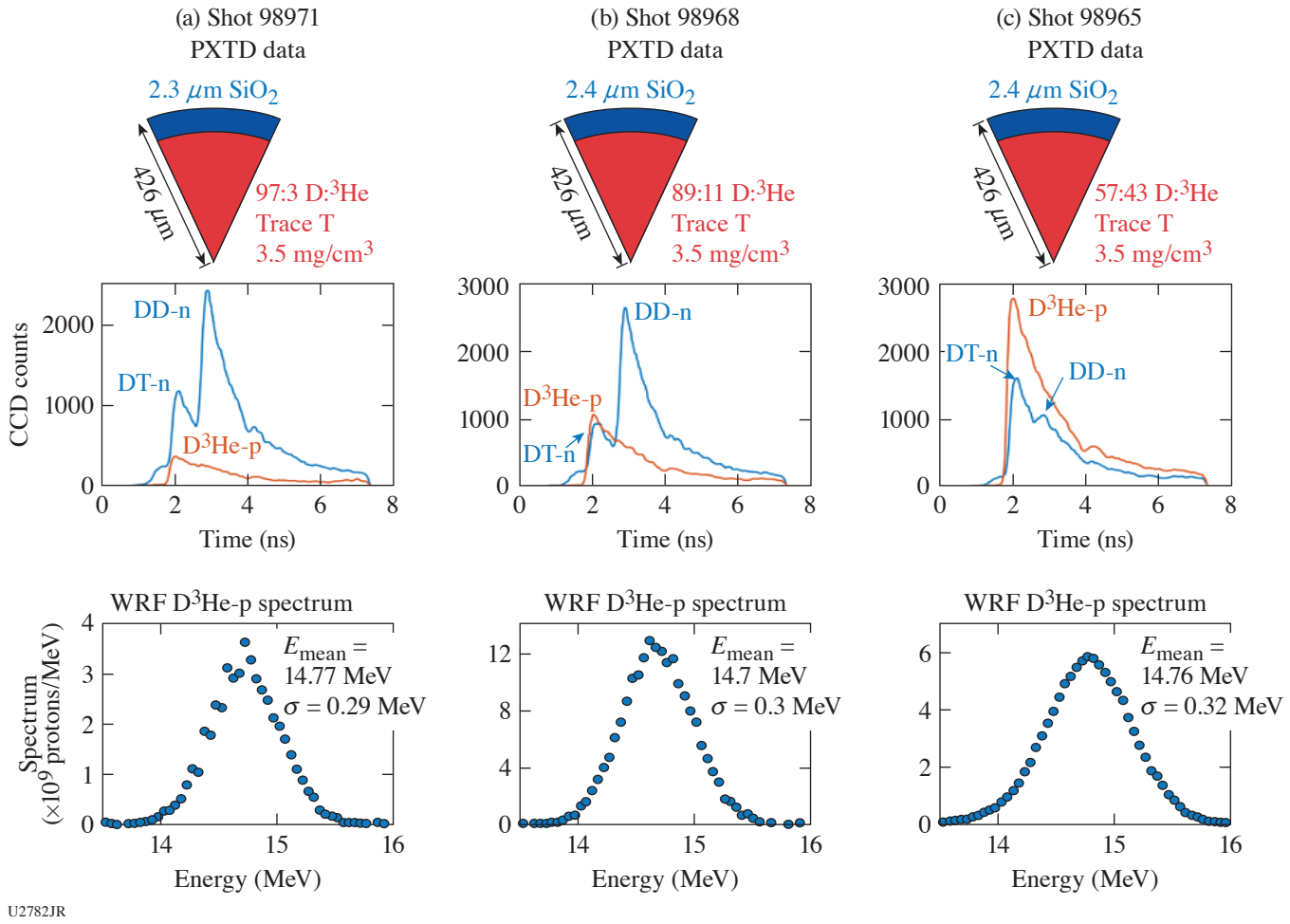

Figure 13
Examples of the PXTD and WRF data collected on the OMEGA shot day PXTD-20B, delayed to FY21. Using the PXTD the DD-n, DT-n, and D^3He-p emission histories were all captured on a single diagnostic, allowing detailed comparison of their relative timing. Direct measurement of the D^3He-p spectrum with WRF's is critical to interpreting this data.

Germanium Dioxide Under Ramp Compression to Extreme Conditions: Phase Transitions in a SiO_2 Analog

Principal Investigators: D. Kim, I. K. Ocampo, and T. S. Duffy (Princeton University); and R. F. Smith and F. Coppari (LLNL)

The high-pressure behavior of AO_2 compounds is of long-standing importance due to their extensive polymorphism and varied transformation pathways. In particular, GeO_2 is one of a family of dioxides whose high-pressure behavior has been of interest as an analog for the behavior of SiO_2 in the deep mantles of terrestrial-type exoplanets. Pressures in the mantles of such exoplanets are expected to exceed 1 TPa, which is far in excess of those attainable in standard static high-pressure experiments. Ramp compression combined with *in-situ* x-ray diffraction (XRD) using the Omega Laser Facility allows one to observe the structure behavior, phase transitions, and kinetics of planetary materials at these conditions.

SiO_2 is expected to adopt low-symmetry crystal structures including the cubic pyrite-type $(Pa\bar{3})$ phase at high pressure and the hexagonal Fe_2P-type or orthorhombic cotunnite-type structures (coordination number of 9). These phases of GeO_2 are predicted

to be stable at lower pressures than in SiO_2 as a consequence of the larger ionic radius of Ge^{4+} relative to Si^4. The challenges in investigating oxide minerals using *in-situ* XRD measurements under dynamic compression are their weak diffraction signal resulting from low-symmetry structures and the low atomic number constituents. In this study, we have examined the high-pressure behavior of GeO_2 under extreme conditions under ramp loading using OMEGA and OMEGA EP lasers.

Sixteen shots on GeO_2 were performed. Polycrystalline α-quartz GeO_2 was compressed to 3 GPa in a diamond-anvil cell producing 10- to 19-μm-thick pellets. The sample pellet was glued between a diamond ablator and either a LiF window for low-pressure experiments (<400 GPa) or a diamond window for high-pressure experiments (>400 GPa). The target assembly was backed by a metal foil with a pinhole material that serves to collimate the x-ray beam. The ramp-shaped laser pulses were used to generate strong compression waves, producing a series of reverberations at layer boundaries in the target package to produce uniform high-pressure conditions in the sample. At predicted peak pressure, a 1- to 2-ns x-ray pulse was generated by irradiating metal foils, and diffracted x rays were recorded on the image plates behind the sample. The velocity at the interface between the sample and LiF window or the free-surface velocity of the rear diamond was measured to determine the stress history within the sample.

We have examined the crystal structure of GeO_2 up to 882 GPa under ramp loading, higher stress than previous studies by a factor of 5. One to five sample diffraction lines were observed from 154 to 882. Our study of GeO_2 shows that pyrite-type GeO_2 occurs from 154 GPa to 436 GPa, which extends to higher pressure than that predicted by theory (~300 GPa). Above 436 GPa, we observe evidence for a post-pyrite phase in GeO_2. Based on the diffraction data, the best candidate for this new phase is the cotunnite-type structure, which has been predicted to be a stable phase of GeO_2 above 300 GPa (Fig. 14). Our results demonstrate that ramp compression can be an effective technique for synthesizing and characterizing dense phases in oxides. Furthermore, we show that ramp compression may also be used to identify lower-symmetry phases in oxide materials. This analog study offers a test of theoretical calculations as well as the crucial information to explore high-pressure behavior of SiO_2.

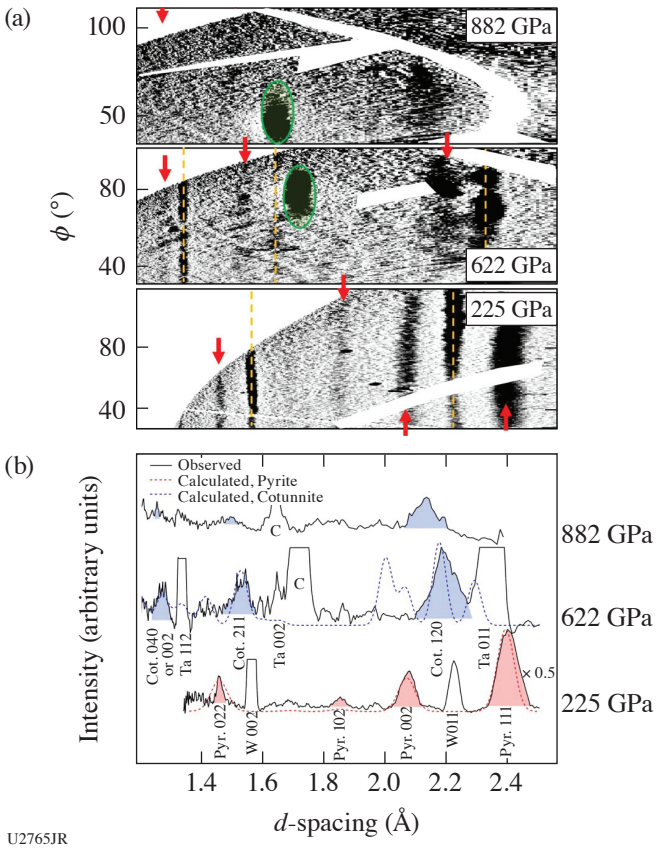

Figure 14
Representative (a) XRD images and (b) integrated 1-D diffraction patterns for ramp-compressed GeO_2. (a) The red arrows indicate the diffraction peaks from the sample. The green ellipses show single-crystal Laue diffraction from diamond that can be identified as highly textured, localized peaks compared to the extended lines of GeO_2.Yellow dashed lines denote diffraction from the pinhole substrate. (b) Pink- and blue-shaded peaks show the observed GeO_2 diffraction lines compared with the calculated diffraction pattern for the pyrite-type structure at 225 GPa (dashed red line) and cotunnite-type structure at 622 GPa (dashed blue line), respectively. The observed diffraction lines at 882 GPa are consistent with the cotunnite phase but could not be calibrated precisely due to the lack of recorded pinhole diffraction signal. "C" denotes a single-crystal spot corresponding to the green ellipse.

Developing Multipurpose Capsule Backlighters

Principal Investigators: C. C. Kuranz, H. J. LeFevre, and K. V. Kelso (University of Michigan)

Many experiments use capsule implosions as x-ray backlighters.[19,20] As x-ray sources, they are bright, short-duration emitters of continuum soft x rays below 10 keV with small spatial extent. With a large physics target, however, it can be difficult to direct beams to the capsule uniformly, and an understanding of the influence of the laser irradiation pattern on the backlighter performance is necessary. Keiter *et al.* addressed this issue in work to observe the duration and spectral content of capsule backlighters with anisotropic laser patterns.[21]

A case can also be made that the capsule backlighters are not being used to their full potential. The capsule implosion, which creates the backlighter, contains a considerable amount of energy and heats the stagnated plasma to kilovolt temperatures with densities significantly above solid density. This is a useful set of conditions and with the appropriate target geometry could create a source that has bright continuum and line emission that would be capable of making two measurements with a single source.

On recent OMEGA shot days, with the participation of graduate student K. V. Kelso and postdoctoral research fellow H. J. LeFevre, we explored capsule backlighters with anisotropic laser irradiation patterns and specifications to produce useful line and continuum emission. The experiments used multiple spectrometers along with framing cameras to diagnose the emission from the capsule. The work on anisotropic laser irradiation patterns expands the work of Keiter *et al.* through the development of a metric to characterize the initial laser pattern on a capsule.

$$\phi = \frac{1}{N_{\mathrm{LOS}}} \sum_{i}^{N_{\mathrm{LOS}}} e^{-\left| 1 - \frac{I_{\mathrm{LOS},i}}{\bar{I}} \right|}, \tag{1}$$

where ϕ is the metric to determine the laser pattern anisotropy, N_{LOS} is the number of lines of sight in the capsule model, $I_{\mathrm{LOS},i}$ is the rms intensity for a particular line of sight, and $\bar{I}$ is the average intensity over the entire capsule surface. This parameter is one where the laser intensity is uniformly distributed over the surface of the capsule and zero when the intensity is localized to very small spots on the capsule. For laser irradiation patterns using VisRad,[22] the value of ϕ is 0.9983 for a 60-beam illumination on OMEGA and 0.9424 for the experiments presented here.

This work creates a dual-source backlighter using a nickel layer on the interior surface of a standard CH vacuum capsule. The thicknesses of the layers are adjusted to keep the mass of the capsule identical to the typical 9-μm wall thickness and 860-μm outer diameter of the commonly used vacuum capsules. This should produce continuum emission in the 2- to 5-keV range, which would be useful as an absorption probe for features near the Ar K-shell and line emission from the Ni K-shell near 7.8 keV. The line emission could act as a pump for fluorescence measurements or as a probe for x-ray Thomson scattering with the correct experimental design. Figure 15(a) shows the capsule specification for the dual-source design.

Spectral measurements using an XRS in ten-inch manipulators TIM-1 and TIM-3 provide some understanding of the uniformity of the emission from these backlighters. Figure 15(b) compares x-ray spectra between two lines of sight using a CH vacuum capsule and time-integrated, flat crystal spectrometers observing emission in the 2- to 4-keV range. The analysis converts the image plate readout to an absolute photon spectrum using a common approach,[19] but it is important to point out that this is only accurate to the image-plate sensitivity, crystal rocking curve, and filter attenuation, which were all calculated and not measured in this work.

The emission from the nickel-lined capsules used the SXS, the imaging x-ray Thomson scattering (IXTS) spectrometer, and an XRS to monitor the line emission. Figure 15(c) shows the Ni K-shell emission from the XRS clearly indicating the presence of bright lines that have similar contrast to laser-irradiated foil targets. Data from the SXS and IXTS confirm these findings and show that the line emission does not extend outside the original bounds of the capsule, but this is not shown here. This may indicate the hot electrons and high-energy photons from the laser–plasma interactions are interacting with the nickel early in time. Figure 15(d) compares the outer diameter of the imploding capsule as a function of time from framing-camera measurements with

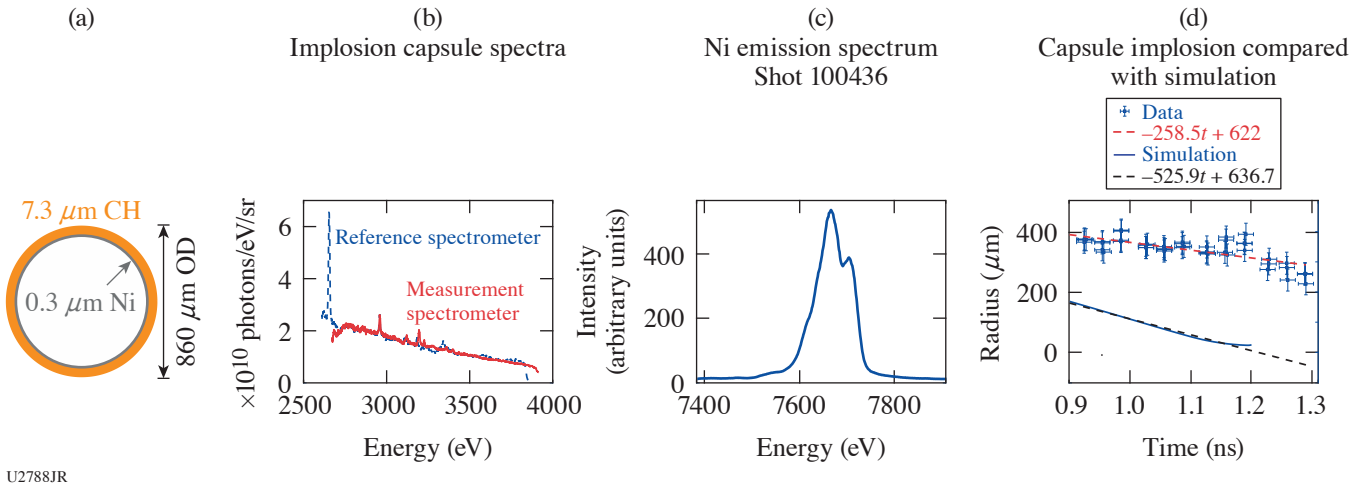

Figure 15
(a) The specified dimensions of the Ni-lined capsules used to produce an x-ray source that has a tailored spectrum to produce line and continuum emissions that are useful for measurements. (b) A comparison of two time-integrated spectrometers viewing an evacuated, CH capsule from TIM-1 and TIM-3 on the same shot. The text provides caveats to the accuracy of the photon number spectrum. (c) The Ni K-shell using an XRS from an experiment using a lined capsule that shows the bright, high-contrast lines that could provide an additional probe for a diagnostic. (d) A comparison of the outer diameter of a Ni-lined capsule implosion between 1-D simulation results and framing-camera data. The difference in the minimum diameter could be due to the 3-D nature of the experiment from the anisotropic laser irradiation pattern.

1-D simulation results. The framing camera used here had an 8×-16 nose cone with a 50-ps pulse forming module (PFM) on a charge-coupled device (CCD). There was also a pair of filters, 10 μm Ni and 12.5 μm Mo, that restricted the transmitted light to the spectral range of the nickel K-shell. This analysis draws circles around the framing-camera images with a threshold for the average pixel to determine the outer boundary of the capsule. The error bars in this figure use the pinhole and motion blurring for the spatial dimension and the PFM and bias voltage for the time axis. This shows that the simulations are reaching a much smaller minimum radius than the experiments. There are many possible reasons for this: The anisotropic nature of the laser irradiation pattern will create a very nonuniform implosion that causes the stagnated plasma to be highly aspherical. Additionally, there is the potential for hydrodynamic instabilities to develop at the interfaces, which will reduce the inward velocity of the nickel flow, resulting in lower compression. These are also 1-D simulations of a problem that will have significant 3-D effects, leading one to expect differences when comparing with experimental results.

This work is funded by the U.S. Department of Energy NNSA Center of Excellence under Cooperative Agreement number DE-NA0003869 and the National Laser User Facility Program.

Collision of Two Magnetized Jets Created by Hollow Ring Lasers
Principal Investigator: E. Liang (Rice University); and H. Ji and L. Gao (Princeton Plasma Physics Laboratory)

The goal of this proposal is to take advantage of the 60 OMEGA laser beams to create and study strong, magnetized, high beta shocks by colliding head-on two supersonic MG magnetized jets created by irradiating flat plastic targets with a hollow ring of laser beams. In our previous OMEGA experiments, we have successfully demonstrated creation of a narrowly collimated plasma jet with MG-level magnetic fields around the jet by irradiating 20 OMEGA beams onto a flat plastic target in a ring pattern.[23] The jet properties were characterized as a function of ring radius d and target composition (pure CH versus 2% Fe-doped CH). The strong MG poloidal magnetic field of these jets is created via the Biermann battery mechanism by the collisions of individual beam blowoffs and compressed by the on-axis flow. The field gets stronger, more ordered, and persists to greater distances from the target as d is increased from 0 to 1200 μm. During FY21, we successfully carried out two OMEGA experiments (one OMEGA only and one joint experiment) to study collision of two such counter-propagating jets and the formation of shocks.

Figure 16 is a sketch of the OMEGA-only experimental setup where 19 OMEGA beams from each of the OMEGA hemispheres irradiated a flat CH target with a hollow ring pattern having an 800-μm ring radius. The jet properties in terms of collimation, flow speed, and magnetic-field generation were optimal in our previous campaigns. The two jets were separated by 6.4 mm. We employed three main diagnostics to characterize the properties and evolution of the collision region near TCC: Thomson scattering (TS), proton radiography, and an XRFC. The TS diagnostic measures the time evolution of density, electron and ion temperatures, and flow velocity at TCC, at 0.15 mm, and 0.25 mm from TCC along the jet axis. Beam 25 was used for TS. For the OMEGA-only experiment, monoenergetic protons generated from D^3He implosions with the rest of the 21 OMEGA beams were used to probe the magnetic-field geometry and magnitude. The primary difference between the OMEGA-only and joint experiments was the proton radiography diagnostic. For the joint experiment, broadband protons generated by intense laser–solid interactions using the OMEGA EP beam were used for proton radiography. The XRFC was used to capture time-lapse x-ray images of the entire domain. We obtained excellent data from all diagnostics for both experiments.

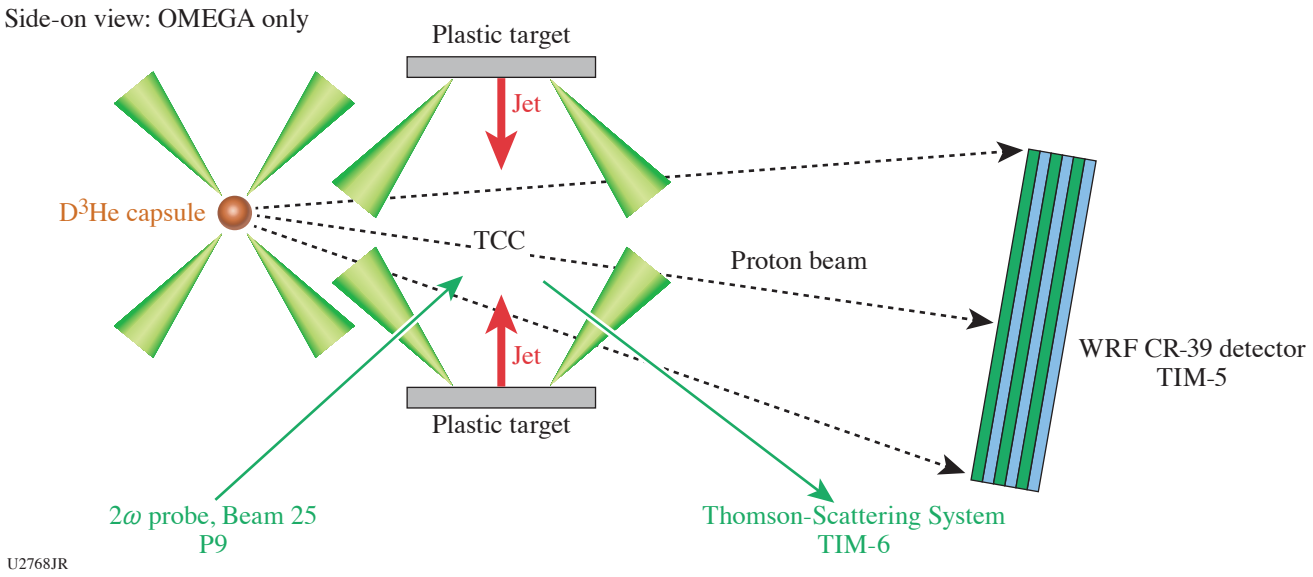

Figure 16
Sketch of the experimental setup for two colliding magnetized jets.

Figure 17 shows the measured XRFC data as a function of time in direct comparison with 3-D *FLASH* simulations. The experimental data show very nicely the jet formation and collision and the shock formation. Because of the assumption of Spitzer electron thermal conductivity in *FLASH*, the electron thermal conduction fronts run far ahead of the shocks. The quasi-isothermal electron temperature profile away from TCC is much hotter than the ion temperature. By comparing the *preliminary* TS, proton radiography (Prad), and XRFC data with 3-D *FLASH* predictions, we arrive at the following tentative conclusions:

1. The XRFC images show that the morphology of the shocked region strongly resembles those predicted by 3-D *FLASH*. The shocked region appears well defined and largely orthogonal to the jet axis as predicted, with only a slight tilt, due to the (unavoidable) small misalignment of the two jets.

2. The TS data at TCC agree very well with 3-D *FLASH* predictions for density, electron, and ion temperatures. This gives us comfort in the performance of 3-D *FLASH* simulations.

3. The TS-derived electron temperature at 0.15 mm below TCC appears, however, *much lower* than 3-D *FLASH* predictions, which was based on Spitzer (2006) electron thermal conductivity. This suggests that the *true electron thermal conductiv-*

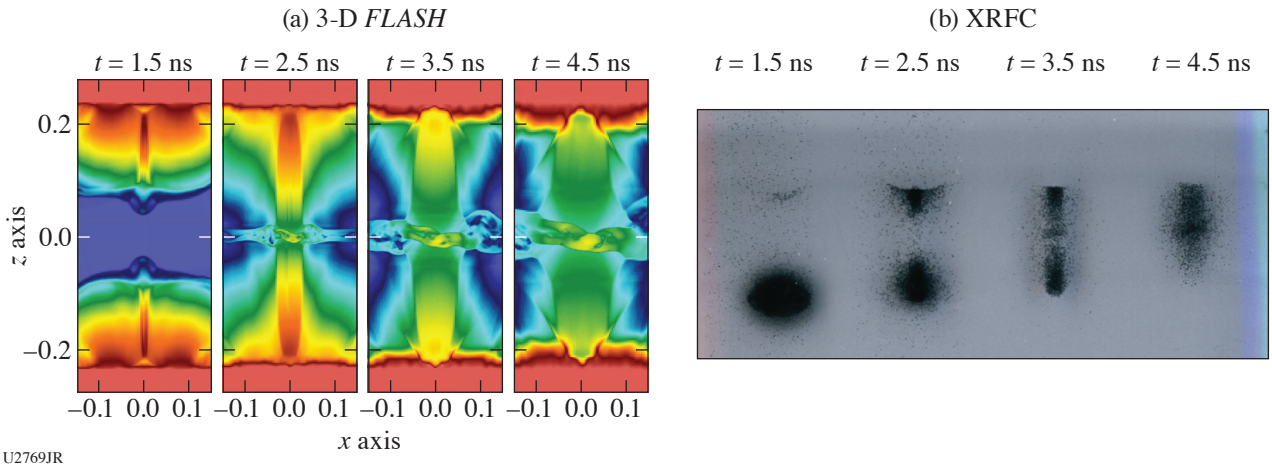

Figure 17
(a) Three-dimensional *FLASH* predictions of the jet and shock morphology largely resemble (b) the XRFC images. Both the simulated and XRFC images show a slight tilt of the shocked region due to the imperfect alignment of the two colliding jets.

ity must be lower than predicted by the Spitzer model, most *likely due to strong magnetic fields orthogonal to the jet axis*, which inhibit electron transport along the flow. Further study using a modified *FLASH* code with *self-consistent* magnetized anisotropic electron transport is in progress.

The Prad data of Fig. 18 shows that, while the fields far from the contact surface remain parallel to the jet axis as in previous single-jet Prad images, *in the region between the shocks, the fields appear to be largely parallel to the contact surface and orthogonal to the jet axis*. This is consistent with *FLASH* predictions. The field direction appears to turn somewhere between the shock and the electron-conduction front positions. We emphasize that our field patterns are completely different from those created by Weibel (1959) instability in the collisionless regime.

This work was supported by the National Laser Users' Facility under Grant No. DOE DE-NA0003942.

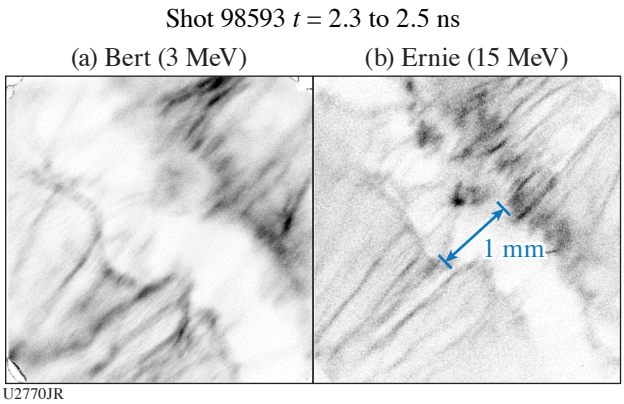

Figure 18
Sample proton images; jet axes run from lower left to upper right.

A Laboratory Photoionized Plasma Experiment on OMEGA EP
Principal Invesigators: R. C. Mancini (University of Nevada, Reno); R. F. Heeter and D. Liedahl (LLNL); and S. P. Regan (LLE)

Photoionized plasmas are widespread in the universe, e.g., active galactic nuclei, warm absorbers, x-ray binaries, and the accreting disks surrounding black holes. The focus of this project is to study in the laboratory the heating, temperature, and

charge-state distribution of photoionized plasmas driven by a broadband intense flux of x rays. Most laboratory work performed to date on laboratory plasmas pertains to collisional plasmas;, i.e., those where electron collisional processes play a dominant role in the plasma ionization and atomic physics. Relatively little attention has been paid, however, to understanding the basic properties of laboratory photoionized plasmas where both photoionization and photoexcitation, driven by a broadband x-ray flux, become dominant. The quantitative information that we obtain from these objects is based mainly on the analysis of spectroscopic observations made by orbiting telescopes such as Chandra and XMM-Newton. The complexities of the astrophysical environment make the spectral analysis challenging, however, and laboratory experiments are critically needed to benchmark analysis codes.

We have established a new experimental platform for OMEGA EP that uses a plastic-tamped silicon sample driven by the 30-ns-duration, broadband x-ray flux produced by the Gatling-gun radiation source. This source is comprised of three copper hohlraums that are sequentially driven by three OMEGA EP beams, each one delivering 4 kJ of UV energy in a 10-ns square pulse shape. Each copper hohlraum has a length of 2.8 mm and an inner diameter of 1.4 mm and is filled with TPX foam. The laser beams sequentially illuminate one hohlraum at a time, thus producing an x-ray flux characteristic of 90-eV radiation temperature for a time period of 30 ns. The relatively long duration of the Gatling-gun radiation source is critical to producing a plasma in photoionization equilibrium where photoionization is counterbalanced by radiative and dielectronic recombination.

The experimental setup has three components: (1) the Gatling-gun x-ray source, (2) a tamped silicon sample, and (3) a titanium backlit source. The silicon sample has a diameter of 2 mm and is placed at a distance of 7 mm from the source. It has an initial thickness of 0.2 or 0.4 μm and is coated on both sides with submicron-thick, 2.5-mm-diam layers of parylene plastic. Heated by the x-ray flux, the tamped silicon sample expands and ionizes into the L-shell range of silicon ions; i.e., neon- to lithium-like ions, thereby producing a photoionized plasma in steady state with an atom number density of a few times 10^{18} atoms/cm^3 and a relatively uniform spatial distribution.

The spatial extension of the blow-off TPX/copper plasma from the copper hohlraums is monitored with the 4ω probe laser to make sure that it does not reach the silicon sample. The silicon photoionized plasma is probed with L-shell self-emission spectra recorded with a grating spectrometer and K-shell line absorption spectra recorded with a KAP crystal streaked spectrometer. The latter is afforded by a 1-ns-duration, separate titanium backlight source driven by the fourth laser beam of OMEGA EP. This laser beam delivers 1 kJ of UV energy onto a titanium slab target in a 1-ns square pulse shape. The radiative recombination continuum emission photons of the titanium laser-produced plasmas backlight and probe the photoionized plasma via absorption spectroscopy. From this measurement, the charged-state distribution and electron temperature of the plasma can be extracted.

Figure 19 displays the transmission spectra recorded in a series of nominally identical experiments where the titanium backlit source was fired at three different times relative to the beginning of the x-ray drive. The Gatling-gun x-ray flux starts at $t = 0$ ns

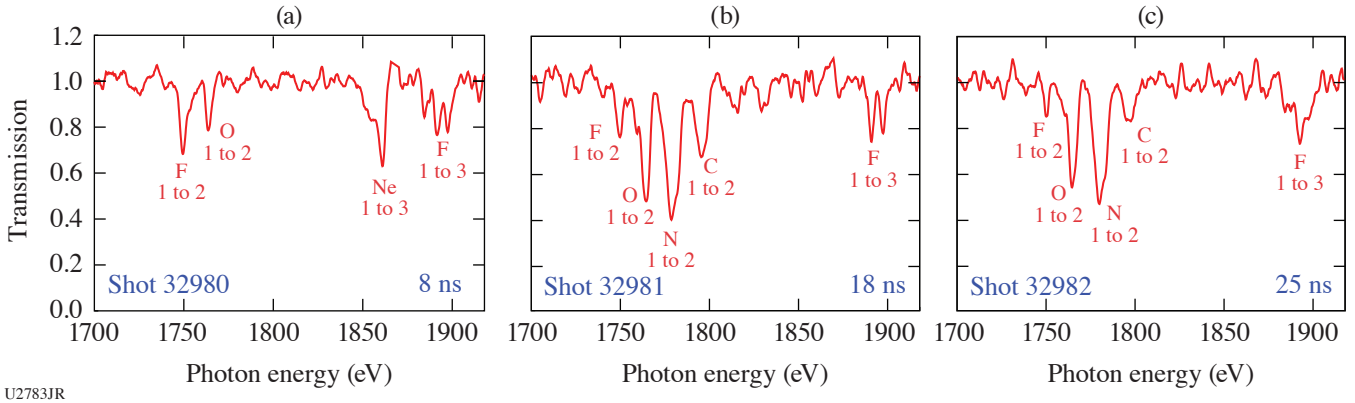

Figure 19
K-shell transmission spectra of the silicon photoionized plasma at (a) $t = 8$ ns, (b) 18 ns, and (c) 25 ns recorded in three nominally identical experiments on OMEGA EP. Shot numbers and line absorption transitions in Ne-, F-, O-, N- and C-like Si ions are indicated in the plots.

and lasts until t = 30 ns. The tamped silicon sample was 0.4-μm thick and tamped on both sides with 0.5 μm of parylene. The data show n = 1 to n = 2 line absorption transitions in F-, O-, N- and C-like silicon ions as well as n = 1 to n = 3 in Ne- and F-like ions. On one hand, the observation at t = 8 ns is characteristic of the end of the initial phase of heating and ionization. It displays a silicon plasma that is just beginning to populate the range of L-shell ions. On the other hand, the transmission spectra recorded at t = 18 ns and t = 25 ns are nearly identical and dominated by n = 1 to n = 2 transitions in F-, O-, N- and C-like silicon ions. These nearly identical measurements demonstrate that a photoionized plasma in steady state has been produced in the laboratory for the first time. The latter is critical to compare with and benchmark the astrophysical modeling codes that are employed in the analysis and interpretation of x-ray astronomy observations.

Measurement of Kinetic Mix Mechanisms Using Separated Reactant Experiments in an Exploding-Pusher Regime
Principal Investigators: B. Reichelt, P. J. Adrian, N. V. Kabadi, C. K. Li, M. Gatu Johnson, and J. A. Frenje (MIT)

The goal of this campaign was to perform measurements of non-hydrodynamic mix mechanisms in exploding-pusher–type targets. Traditionally, ICF design has been chiefly driven by hydrodynamic simulations that have no models implemented to describe mixing of one material into another. During shock propagation, however, the high temperatures reached by ions challenges this assumption and can lead to situations where diffusion is the predominant source of mix, rather than hydrodynamic instabilities like Rayleigh–Taylor and Richtmyer–Meshkov. This work attempted to probe this effect using a CD shell with an inner CH offset of varying thickness and a ^{3}He fill, so that D^{3}He-p observed must come through diffusion from the CD layer into the hot spot [Fig 20(a)]. The setup was similar to previous work done by Meany *et al.*[24] but extended to lower fill pressures and capsule thicknesses in order to capture a more exploding-pusher–like regime where a kinetic description of mix becomes necessary. Unfortunately, when the capsules were glued to the stalks, the glue spots were made out of spec and much too large [Fig 20(b)]. Since large glue spots introduce hydrodynamic mix mechanisms, it is nearly impossible to disentangle the cause of observed yields, so the physics goals of the experiments were compromised. The Omega scheduling facility has recognized this and has been working with us to schedule contingency shots to rectify this issue.

This material is based upon work supported by the Department of Energy, National Nuclear Security Administration under Award Nos. DE-NA0003868 and DE-NA0003938.

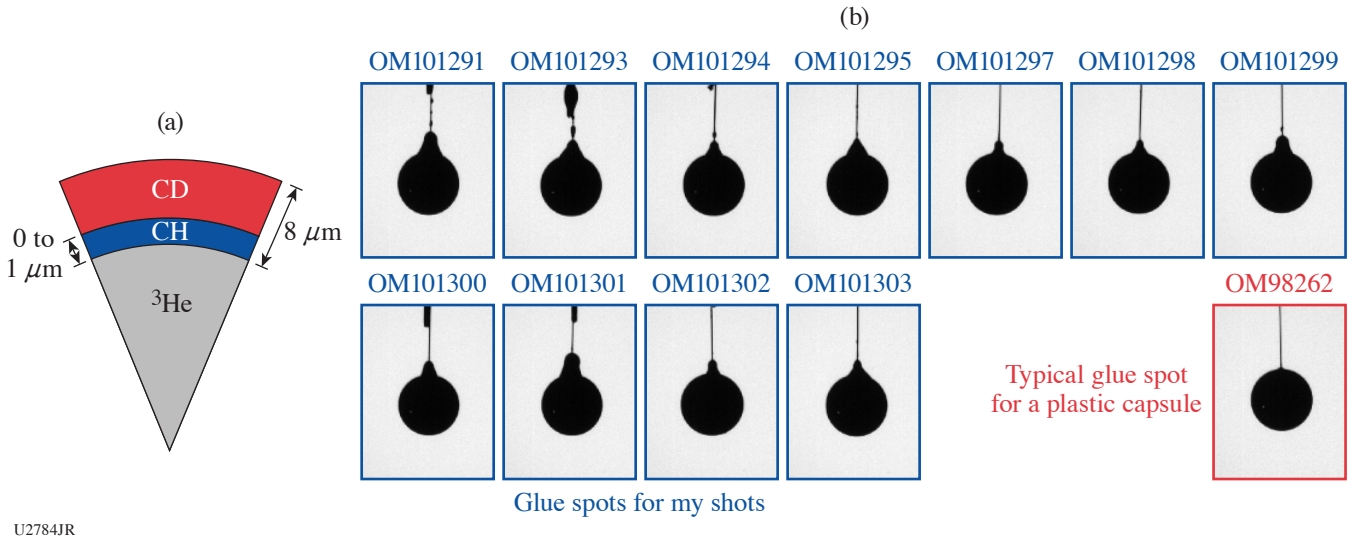

Figure 20
(a) A pie diagram illustrating the target design used for this set of experiments; (b) an illustration of the large glue spots that compromised the physics goals of this campaign.

The Dynamics of Magnetic Fields and Relativistic Electrons in Solid Target Interactions Using OMEGA EP

Principal Inverstigators: B. K. Russell, P. T. Campbell, G. Fiksel, H. Tang, A. G. R. Thomas, L. Willingale, and K. Krushelnick (Gérard Mourou Center for Ultrafast Optical Science, University of Michigan); C. Dong (Princeton Plasma Physics Laboratory); C. A. Walsh (LLNL); and P. M. Nilson (LLE)

The strong magnetic fields produced during the interaction of lasers with solid-density targets have been used to study many processes in the laboratory including magnetic reconnection. The standard reconnection geometry uses two laser pulses interacting on a target to produce expanding plasma plumes with azimuthal magnetic fields.[25] These fields expand with the plumes and are antiparallel, allowing them to reconnect. Several experiments have been performed in this geometry with moderate intensity pulses studying reconnection dynamics including those in asymmetric reconnection.[26] Much higher intensity pulses have also been used, generating relativistic magnetized electrons that reconnected in the first demonstration of relativistic electron-driven magnetic reconnection.[27] On our first OMEGA EP shot day of FY21, we combined these ideas using a moderate intensity pulse and a relativistic intensity pulse to generate a highly asymmetric interaction. On our second OMEGA EP shot day, we explored a slight modification of this geometry with overlapped pulses similar to what has been used in studies for fast-ignition fusion.[28]

We explored two geometries using interactions with foil targets: an asymmetric magnetic reconnection geometry and an overlapped short-pulse/long-pulse geometry. In the reconnection geometry, a 1-ns UV pulse was focused to an intensity of $\sim 10^{14}$ W/cm^2 on thin CH foils, 750 ps before the arrival of a short 500-J, 10-ps IR pulse with an intensity $>10^{18}$ W/cm^2 focused at various separation distances from the long-pulse focus. In the overlapped geometry, these same pulses were used; however, the short pulse was focused to the same position on the target as the long pulse [Fig. 21(a)] and CH and Cu foils were used. In

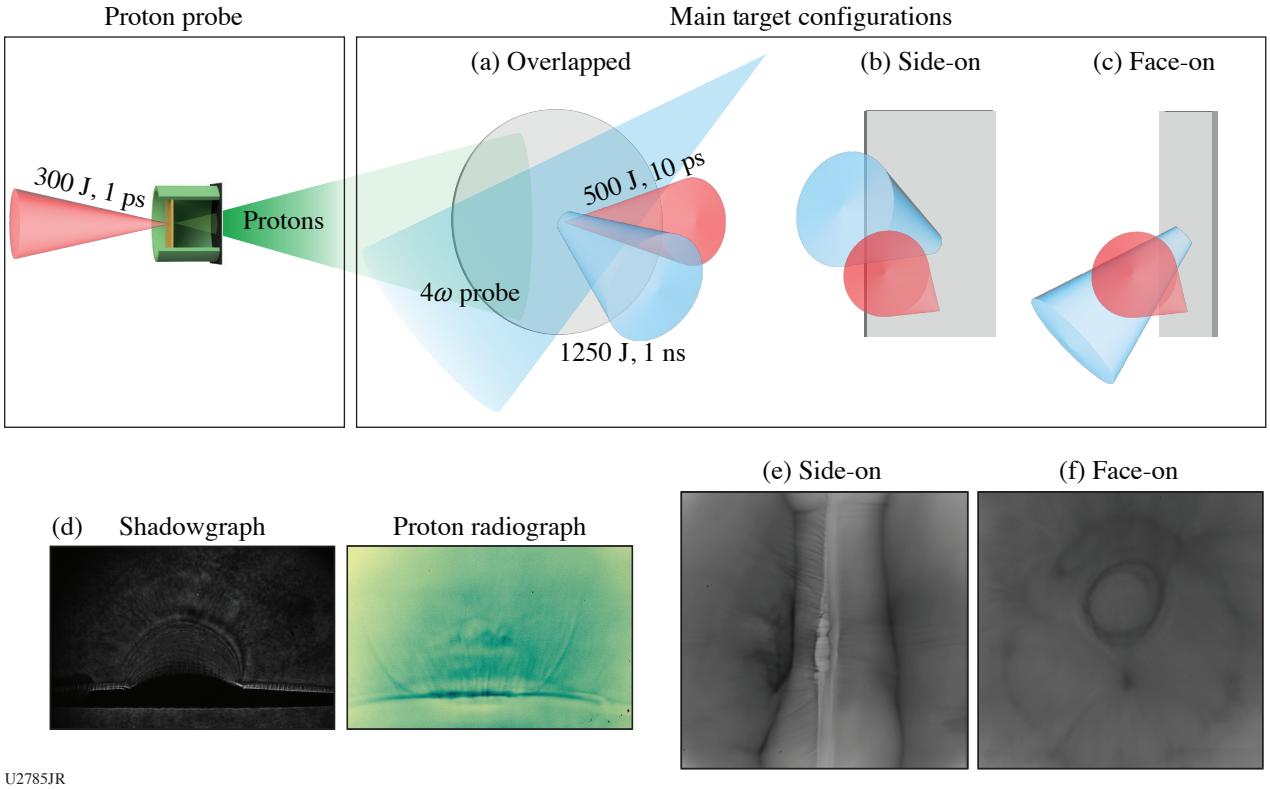

Figure 21

Main target configurations used in our two shot days in FY21 including (a) overlapped, (b) side-on, and (c) face-on. (d) The overlapped configuration allowed for simultaneous probing by the 4ωprobe and protons. The (e) side-on and (f) face-on configurations show the fields in the interaction of the strongly magnetized relativistic electrons with the long-pulse plasma plume.

both geometries, protons were accelerated from Cu foils by a short-pulse 300-J, 1-ps laser and used to probe the interactions.[29] The protons were detected on a radiochromic film (RCF) stack, producing a time series of data on each shot. In the overlapped geometry, the 4ω probe was used to probe the interaction through polarimetry, shadowgraphy, and angular filter refractometry.

In the reconnection geometry, protons were used to image the fields with probing directions normal or transverse to the target surface [Figs. 21(b) and 21(c)], giving us a detailed picture of the interaction. Initially, the long-pulse laser produced a plasma plume with azimuthal magnetic fields generated by the Biermann battery mechanism, $\partial B/\partial t \propto \nabla T_e \times \nabla n_e$ (Ref. 30). The short-pulse then interacted with the foil at separation distances from the long-pulse focus of 1.25 to 2.65 mm, generating strongly magnetized relativistic electrons that expanded from the focal region. On the time scale of the relativistic electron expansion, the long-pulse plume is effectively a stationary magnetized obstacle. In the proton images, we see the formation of bow-shock–like features [Figs. 21(e) and 21(f)]. To understand these features, we performed a massive 3-D particle-in-cell simulation using the code *OSIRIS*[31,32] on the NASA Pleiades supercomputer using ~2.5M core hours. To reduce computation time, the long-pulse plasma plume was initialized in the simulation by fitting to the data obtained from extended-MHD simulations using the code *GORGON*.[33] Additionally, we have been using particle-tracking codes to generate synthetic radiographs of the simulation data. Analysis of the experimental and simulation data is ongoing.

On our most-recent shot day, we explored the interaction in the overlapped geometry shown in Fig. 21(a). A similar setup was used by Ivancic;[30] however, in our shot day, we used proton radiography to study the interaction in addition to the 4ω probe diagnostics. This allowed us to obtain information on both the density and fields in the interaction [Fig. 21(d)]. Shots were taken on Cu and CH, allowing us to study the effects of target material. The delay of the 4ω probe was varied, allowing us to observe the propagation of the short pulse into the long-pulse–generated plume. Analysis similar to that performed for the reconnection geometry will be performed for these data.

This material is based upon work supported by the Department of Energy, National Nuclear Security Administration under Award No. DE-NA0003954. P. T. Campbell is supported by the U.S. Department of Energy Fusion Energy Sciences Postdoctoral Research Program administered by the Oak Ridge Institute for Science and Education (ORISE) for DOE. ORISE is managed by Oak Ridge Associated Universities (ORAU) under DOE Contract No. DE-SC0014664. B. K. Russell acknowledges support from National Science Foundation (NSF) Grant No. 1751462.

Particle Heating by Collisionless Shocks in Magnetized High-Energy-Density Plasmas

Principal Investigators: D. B. Schaeffer (Princeton University)
Co-investigators: W. Fox and S. Malko (Princeton Plasmas Physics Laboratory); G. Fiksel (University of Michigan); and P. V. Heuer (LLE)

Magnetized collisionless shocks, in which the shock forms in a pre-existing magnetic field, appear in many space and astrophysical environments, including planetary shocks, supernovae remnants, and galaxy clusters. Of particular interest are high-Mach-number shocks, which are a key component of astrophysical plasmas and have been associated with extremely high-energy cosmic rays. These strongly driven shocks employ fundamentally different dissipation mechanisms compared to low-Mach-number shocks, resulting in a critical outstanding problem in shock physics: How is energy partitioned among particle populations across high-Mach-number shocks? Despite decades of *in-situ* studies by spacecraft, telescope observations, and corresponding numerical simulations, there remains a lack of understanding of the mechanisms by which particles are heated.

Through the AIBS Program, we carried out two experiments to study particle heating by magnetized collisionless shocks: one shot day on OMEGA and one shot day on OMEGA EP. In the OMEGA shots (MagShkHeat-21A), an external magnetic field was provided by MIFEDS-powered coils (similar in design to the "racetrack" coils used in previous shots[34,35]), a background plasma was produced by ablating a CH foil, and the shock was driven by ablating a second CH foil to drive a piston plasma through the magnetized background plasma [see Fig. 22(a)]. The goals of the OMEGA shots were to measure electron and ion heating with Thomson-scattering diagnostic along two directions and to test the use of a gas jet. The Thomson-scattering diagnostic was set up to probe either parallel or perpendicular to the external magnetic field in order to measure the corresponding parallel or perpendicular heating. A third configuration replaced the background CH foil with a gas jet to test if the gas jet could provide a

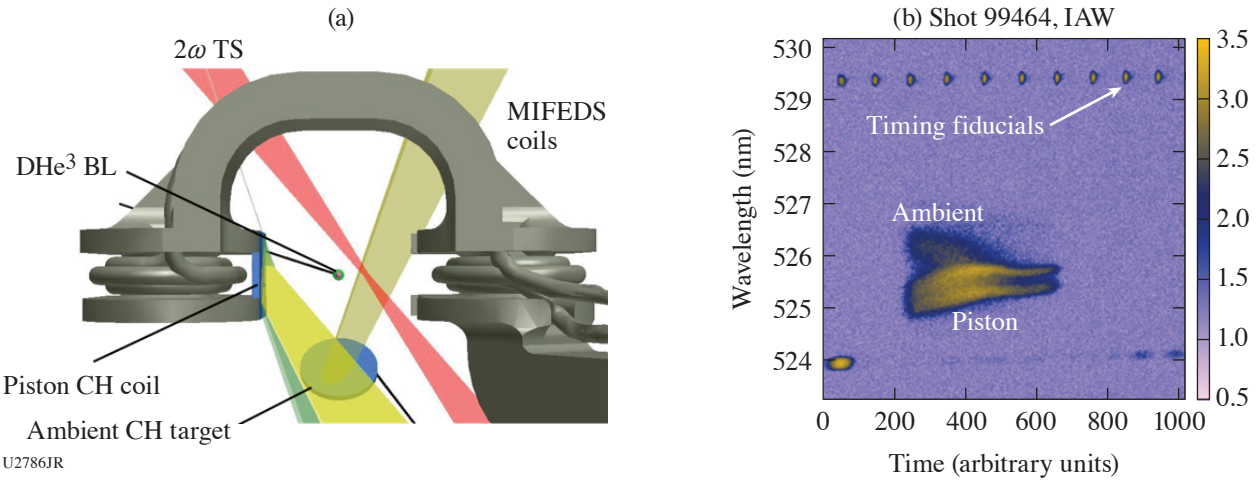

Figure 22
(a) Schematic of the experimental setup on OMEGA for probing perpendicular to the background magnetic field with Thomson scattering. By rotating the MIFEDS coils 90°, the Thomson-scattering diagnostic probed parallel to the field. The ambient CH target was replaced with a gas jet on some shots. (b) Example ion-acoustic wave (IAW) spectrum from the Thomson-scattering diagnostic.

better magnetized background plasma. We successfully acquired Thomson-scattering data in all three configurations, shown in Fig. 22(b). The data are currently being analyzed.

For the shot day on OMEGA EP (MagShkHeat-EP-21A), we designed a brand new MIFEDS-based platform [see Fig. 23(a)], with the goal of providing a more-uniform magnetized ambient plasma and larger magnetized system size. Instead of racetrack coils, we used a Helmholtz coil design, which allowed us to create large fields (~10 T) over several millimeters. The ambient plasma was created by ionizing the gas from a gas jet. Together, this platform allowed us to drive more-uniform shocks over much longer lengths and time scales than what we could achieve previously. The goals of the OMEGA EP shots were to validate this new platform and measure shock spatial scales as a function of shock speed (Mach number). The primary diagnostics were refracting imaging using the 4ω probe beam and proton deflectometry using short-pulse–driven TNSA (target normal sheath acceleration) protons. We also placed an image plate at the back of the proton RCF stack to capture an *in-situ* x-ray reference image of the mesh, which could then be compared to the proton image of the mesh to directly measure the proton deflections.

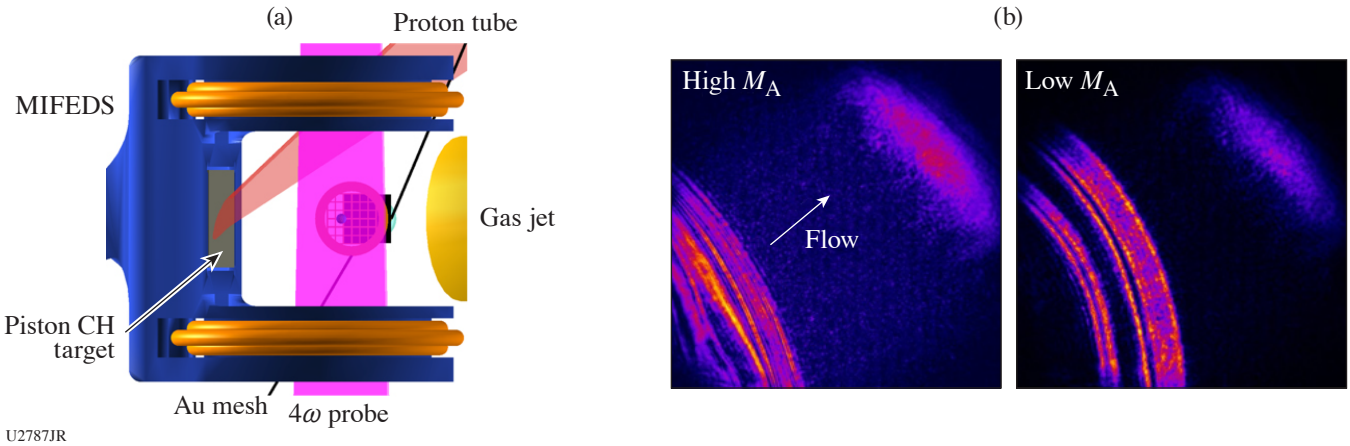

Figure 23
(a) Schematic of the experimental setup on OMEGA EP. (b) Example angular filter refractometry images for two shock Mach numbers.

We successfully demonstrated that the gas jet was compatible with the MIFEDS coils, although the coils were perturbed slightly by the gas pressure. We also successfully demonstrated for the first time that we could acquire a high-contrast *in-situ* x-ray reference image of a mesh.[36] We could only test this on one shot, however, since the gas pressure pushed the mesh into the proton tube. We nonetheless acquired excellent proton images (without mesh) on the remining shots, as well as excellent shadowgraphy and angular filter refractometry images of the shock for several Mach numbers [see Fig. 23(b)]. There are clear variations in the shock structure with a Mach number, which we are currently analyzing.

This work was conducted at the Omega Laser Facility and funded under the auspices of the U.S. Department of Energy by the University of Rochester's Laboratory for Laser Energetics under Contract No. DE-NA0003856. This work was also supported by NASA under Grant No. 80NSSC19K0493.

Investigation of Hydrodynamics and Magnetic-Field Saturation in Foam-Lined Interfaces

Principal Investigators: G. D. Sutcliffe, T. Johnson, J. Pearcy, B. Lahmann, P. J. Adrian, N. V. Kabadi, M. Gatu Johnson, R. D. Petrasso, and C. K. Li (MIT); B. Pollock and J. Moody (LLNL); and J. Katz (LLE)

In ICF hohlraums, prior configurations used gas-filled hohlraums to slow the expansion of high-Z–ablated wall material into the path of the laser beams. This gas-fill technique has largely been abandoned on the NIF because it gives rise to large laser–plasma interactions. Other techniques have been proposed to counteract the expansion of the wall material, including foam-lined hohlraums.

Magnetic fields generated by the interaction of ~ns lasers with foam-lined hohlraums could give rise to magnetic-field saturation, which scales differently than typically seen in experiments with solid-density targets.[37] When the target material is solid density, the ablated plasma exists in the "convective regime" of magnetic-field saturation, where $L/d_i > 1$ and peak magnetic fields are proportional to d_i/L (where d_i is the ion inertial length and L is the temperature-gradient length scale). When plasmas are generated from a foam material, the length scales can approach a different regime: a resistive dissipation regime, where $L/d_i \lesssim 1$ and the peak field goes as L/d_i. Pre-shot *FLASH* simulations of such a configuration corroborated this intuition: regions of Biermann magnetic-field generation have L/d_i of the order of unity, as seen in Fig. 24.

An example target can be seen in Fig. 25(a). Key diagnostics in this experiment are proton radiography to measure magnetic fields and Thomson scattering to measure plasma conditions. Time-staggered proton radiography shots characterize the instantaneous magnetic fields at a variety of times. Imaging Thomson-scattering data were acquired to characterize instantaneous density

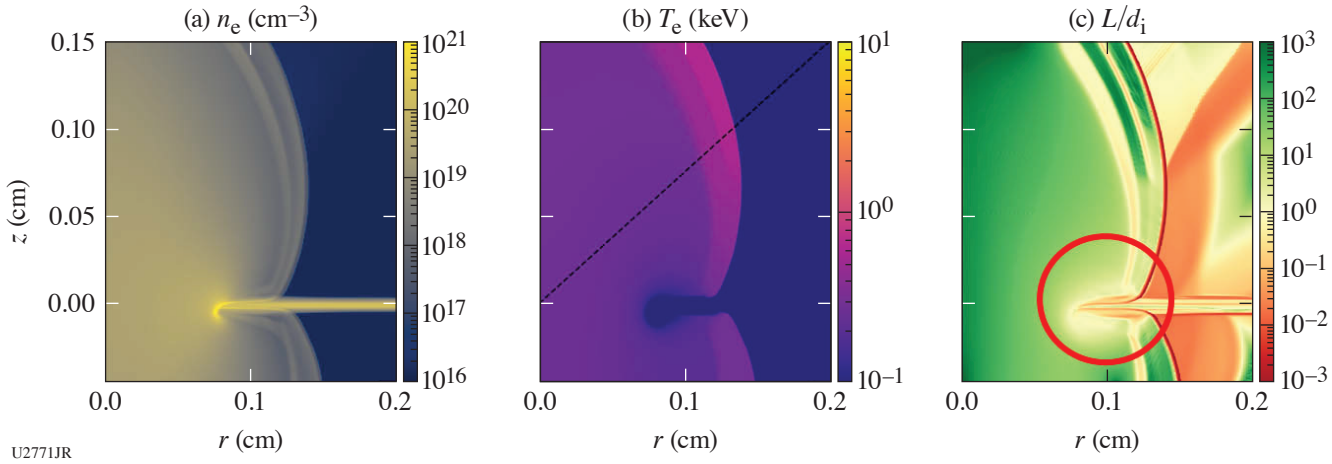

Figure 24

FLASH simulations showing the expected (a) electron density, (b) electron temperature, and (c) normalized length scale (L/d_i). In the region where Biermann fields are generated, L/d_i is of the order of unity.

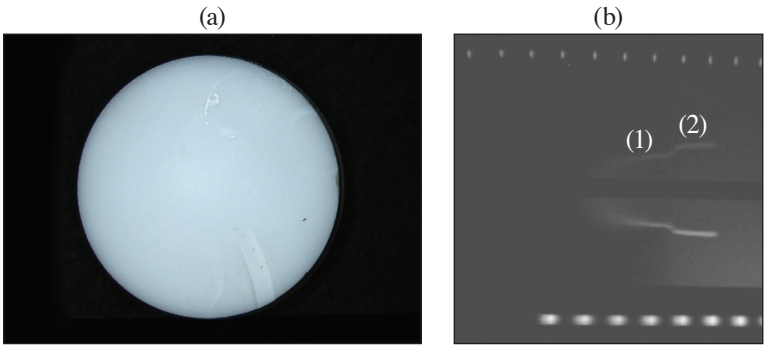

U2772JR

Figure 25
(a) One of the 50-mg/cm^3 foam targets, viewed face-on. (b) Thomson-scattering electron plasma wave data showing the evolution of plasma density in the region above the foil surface. At (1), we see the low-density material ablating from the foam portion of the target. In (2), the bubble is shocked by the ablation of the solid-density backing material expanding into the earlier bubble.

and temperature profiles in the ablated plasma region. The processing of proton radiography CR-39 detector data is underway. Interesting shock features can be seen in the Thomson-scattering data [Fig. 25(b)], which match *FLASH* simulations where a solid-density backing was included. Combined analysis of proton radiographs, Thomson-scattering data, and *FLASH* simulations is underway.

This work was supported in part by the National Laser Users Facility under Contract DE-NA0003938.

Relativistic Intensity Laser Channeling and Direct Laser Acceleration of Electrons from an Underdense Plasma
Principal Investigators: H. Tang, A. McKelvey, P. T. Campbell, B. K. Russell, Y. Ma, A. G. R. Thomas, and L. Willingale (University of Michigan); J. L. Shaw and P. M. Nilson (LLE); H. Chen and F. Albert (LLNL); and A. V. Arefiev (University of California, San Diego)

Laser–plasma interactions generate high-energy electrons, which have a number of applications, including generating secondary sources like x-ray radiation, electron–positron pairs, ion acceleration, or neutron generation. Direct laser acceleration (DLA) is one mechanism for producing these relativistic high-energy electrons. The transverse electric field of the laser pulse accelerates electrons too close to the speed of light, and the $v \times \mathbf{B}$ force converts electron transverse momentum to longitudinal momentum. If the interaction occurs within an underdense plasma, the localized electric and magnetic fields of the laser channel can significantly enhance the electron energy gain.[38,39] Our experiments aim to understand the dynamic and complex DLA mechanism to optimize the high-energy electron beam production. During two shot days in FY21, we performed a series of shots to investigate the effects of the *f* number, laser pulse duration, and plasma density.

A backlighter short laser pulse with a 1053-nm wavelength was focused onto the edge of a 2-mm-diam helium gas-jet target. The backing pressure to the gas jet was varied to adjust the plasma density of the interaction. The laser pulse duration was varied between 1 to 5 ps, and the beam was apodized to alter the *f* number (and therefore the focal-spot size). The generated hot electrons were measured by a laser-axis EPPS and a transverse EPPS. The 4ω optical probe was employed to map the plasma density profile. The quasi-static electric- and magnetic-fields evolution of the plasma channel was observed using proton deflectometry. The proton probe was generated using the 1-ps sidelighter beam and a 50-μm Cu foil. To improve the temporal resolution of proton radiography, we used a customized RCF pack.

A laser channel is observed in the 4ω shadowgraph shown in Fig. 26(a). The laser is propagating from the left to the right. The proton probe beams deflected by the fields of the channel are shown in an example RCF image [Fig. 26(b)]. The laser creates a clean channel through the plasma, and filaments surround the main channel and expand to a goblet shape. For a pulse with a longer duration like 3 ps and 5 ps, the extended time of the pulse's existence in the plasma prevents electrons from moving back from the upper and lower walls to the channel, leading to a wider and more-uniform main channel and more-confined filaments.

Figure 26(c) shows the electron spectra from the laser-axis EPPS. The solid and dashed curves represent two shot series using different gas nozzles. Due to a reduced aperture size for the large apodizer, the laser energy for a large *f* number is smaller. Despite

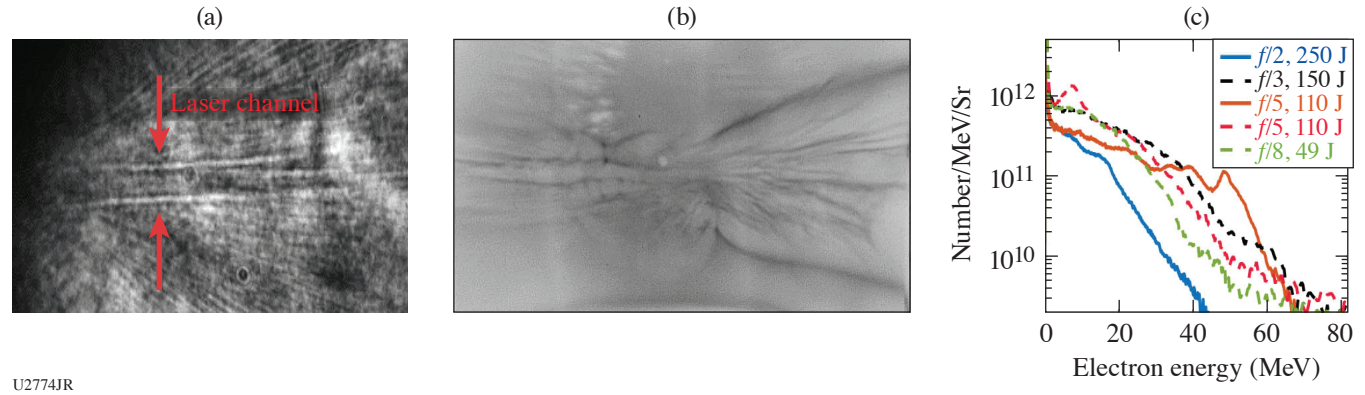

Figure 26
(a) A 4ω shadowgraph image from shot 35722. The laser is propagating from the left to the right and the channel walls are between the arrows. (b) The raw RCF image from shot 35722 illustrates the deflections in the proton beam caused by the channel fields. (c) Electron spectra for various focusing geometries.

the reduction in laser energy, and therefore intensity, the mean electron energy with a large *f* number does not drop significantly for these conditions. The electron acceleration was likely affected by the size of the laser focal spot. We are conducting PIC simualtions to investigate the effects of focal-spot size, density, and laser pulse duration.

This material is based upon work supported by the DOE/NNSA under Award Number DE-NA0003944.

Fundamental Astrophysical Processes in Radiative Supersonic Magnetohydrodynamic Turbulence

Principal Invesitgators: P. Tzeferacos,*§ A. Reyes, Y. Lu, K. Moczulski,* P. Farmakis,* and A. Armstrong* (Flash Center for Computational Science, University of Rochester); C. Palmer (Centre for Plasma Physics, School of Mathematics and Physics, Queen's University, Belfast); A. F. A. Bott (Department of Astrophysical Sciences, Princeton University); H. Poole and G. Gregori (Department of Physics, University of Oxford); D. H. Froula and J. Katz (LLE); A. Birkel, C. K. Li, and R. D. Petrasso (Plasma Science and Fusion Center, MIT); J. S. Ross and H.-S. Park (LLNL); and D. Lamb (Department of Astronomy and Astrophysics, University of Chicago)
*Also LLE
§Also Department of Physics, University of Oxford

Magnetic fields are ubiquitous in the universe and are salient agents in numerous astrophysical processes;[40] however, their origin is not fully understood. The consensus among cosmologists and astrophysicists is that cosmic magnetic fields are the result of dynamo amplification of tiny seed fields in turbulent magnetized plasmas.[41] The turbulent dynamo mechanism eluded experimental demonstration for decades, while theoretical and numerical studies largely relied on simplified models[42] that steer clear of realistic magnetized compressible turbulence, where strong density fluctuations, shocks, filamentation, and radiative effects complicate the picture and confound the analysis. This project aims to demonstrate and characterize fluctuation dynamo in compressible, radiative plasmas in a controlled laboratory environment. The experiments exploit the mature TDYNO experimental platform we developed[43] for the Omega Laser Facility and demonstrated turbulent dynamo in the laboratory for the first time[44] and it was meticulously characterized.[45] The experiments also build on the experience we have gained in designing and interpreting laser-driven experiments using validated simulations created with *FLASH*,[46] a highly capable radiation MHD code we have developed that is able to simulate a wide range of high-energy-density physics experiments.[47] The project establishes a basis for laboratory investigations on the nature of the saturated MHD turbulent state in radiative, compressible turbulence.

The second shot day of our OMEGA campaign was carried out on 15 July 2021 and was geared toward measuring (1) the plasma viscosity using the spectral cutoff of the density fluctuations and (2) the self-emitted fusion protons in the plasma due to D–D reactions. The platform deployed is shown in Fig. 27(a) and is similar to the one we fielded at Omega for our previous suc-

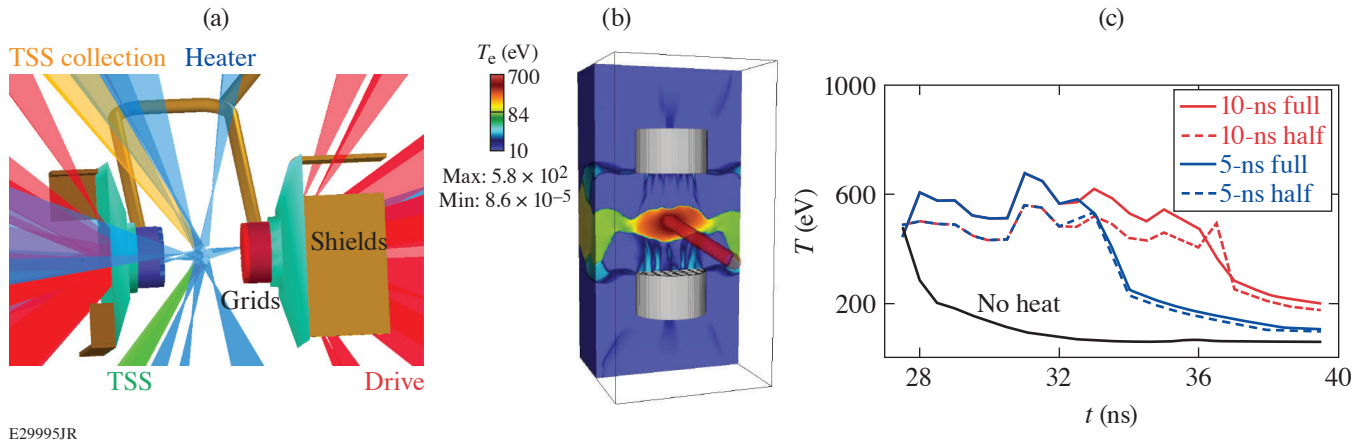

Figure 27
Turbulent dynamo experiments at Omega. (a) VISRAD schematic of the TDYNO platform for OMEGA to study the viscous cutoff in the power spectrum of the turbulent plasma. (b) *FLASH* simulation of the experiment showing one of 11 heater beams heating the turbulent plasma (electron temperature rendering, eV). (c) Temporal profiles for different heater-beam configurations showing the plasma temperatures (eV) that the turbulent interaction region can sustain.

cessful TDYNO campaigns. The assembly is comprised of two composite targets and two grids that are connected by a pair of cylindrical shields. The composite targets are 3 mm in diameter and consist of a 50-μm-thick deuterated polystyrene foil (CD) and a 240-μm-thick polystyrene washer. The polystyrene washers were machined to have a 400-μm-diam cylindrical "well" in their centers. The two targets are mounted 8 mm apart and the pair of grids is placed between them. The two grids are made of polyimide and are mounted 4 mm apart—each of them 2 mm away from the respective proximate face of the foil target. The 3-mm-diam, 230-μm-thick grids consist of 300-μm-wide holes and 100-μm wires, offset with respect to each other to break the mirror symmetry of the assembly: grid A (red) has a hole in the center, while grid B (blue) does not. Rectangular cones on each target shield the diagnostics from the intense x-ray emission produced when a sequence of ten 1-ns-duration laser beams coming from different angles illuminate each target. The two targets are driven for 10 ns, delivering a total of 5 kJ per target on an area defined by the laser's SG5 phase plates. The temporal profile of the drive is a flattop profile. As shown in the *FLASH* simulation we performed for the platform design, the beams drive a pair of counter-propagating, high magnetic Reynolds number Rm plasma flows that carry the seed magnetic fields generated by a Biermann battery. The flows propagate through a pair of grids that destabilize the flow and define the driving scale of the turbulence (L). The flows then meet at the center of the chamber to form a hot, turbulent interaction region [Fig. 27(b)], where the magnetic fields are amplified to saturation values. After its formation, the interaction region is also illuminated with a sequence of 11 heater beams (Fig. 27), time staggered for 9 ns, capable of delivering a total of 1.7 kJ. The heater beam configuration can maintain high plasma temperatures for the duration of the illumination [Fig. 27(c)], which alters the plasma viscosity, increases the length scale of the viscous cutoff of the power spectrum, and boosts the yield of DD protons generated in the deuterated plasma.

To measure the turbulent spectrum using x-ray imaging and capture the viscous scale where the turbulent kinetic energy dissipates into heat, we fielded two x-ray framing cameras, one with 2× magnification viewing the turbulent plasma edge-on [Figs. 28(a) and 28(b)], and another with 12× magnification viewing the interaction region at an angle (i.e., our main diagnostic for the viscous length scale). Unfortunately, the 12× magnification camera worked only for the first shot of the day, which significantly impacted the shot rate for the remainder of the experiment and compromised our ability to achieve our scientific objectives. Despite numerous attempts to troubleshoot the high-resolution framing camera problem, we were unable to use our main plasma diagnostic. Nevertheless, the heater beams were, in fact, able to significantly increase the plasma temperature. The 4ω Thomson-scattering diagnostic [Fig. 27(a)] yielded detailed information about the plasma state (ion and electron temperatures, bulk flow velocity, turbulent velocity, and electron density). More specifically, it revealed that we sustained ion temperatures of $\sim$500 eV and electron densities of $\sim 5 \times 10^{19}$ cm^{-3}. For moderate to large fluid Reynolds numbers (Re) periodic box simulations, the viscous cutoff is shown to satisfy

$$kL/2\pi \sim 0.2\,\mathrm{Re}^{3/4},$$

where k is the wave number and L is the driving scale of the turbulence. For our experimental conditions, we have

$$\mathrm{Re} \sim 130\left(\frac{T_\mathrm{i}}{500\,\mathrm{eV}}\right)^{-5/2}\left(\frac{n_\mathrm{e}}{10^{20}\,\mathrm{cm}^{-3}}\right) \sim 50,$$

which is consistent with the reduction we see in relative intensity fluctuations [Figs. 28(c) and 28(d)] and brings the cutoff to $l_\mathrm{visc} > 50\ \mu$m; i.e., above the resolution limit of the 2× magnification framing camera, also shown in the shift toward larger scales of the spectral peak in Figs. 27(e) and 27(f). This preliminary analysis is encouraging and builds confidence for our next shot day, where we expect to have the high-resolution framing camera issues resolved. Finally, we were able to measure the signal on the EPPS diagnostic for two of the shots. Further analysis of the signal, combined with measurements with the proton core imaging spectrometer (PCIS) CR-39, will be used to determine the utility of the signal for benchmarking the DD proton production in the experiment. Despite the complexity of the experimental platform and the experimental diagnostic problems, with the help of LLE personnel, we were able to perform nine shots during this shot day.

The research leading to these results has received funding from the European Research Council (ERC) under the European Community's Seventh Framework Programme (FP7/2007-2013)/ERC Grant Nos. 256973 and 247039, DOE NNSA under Contract No. B591485 to LLNL, Field Work Proposal No. 57789 to Argonne National Laboratory (ANL), Subcontract No. 536203

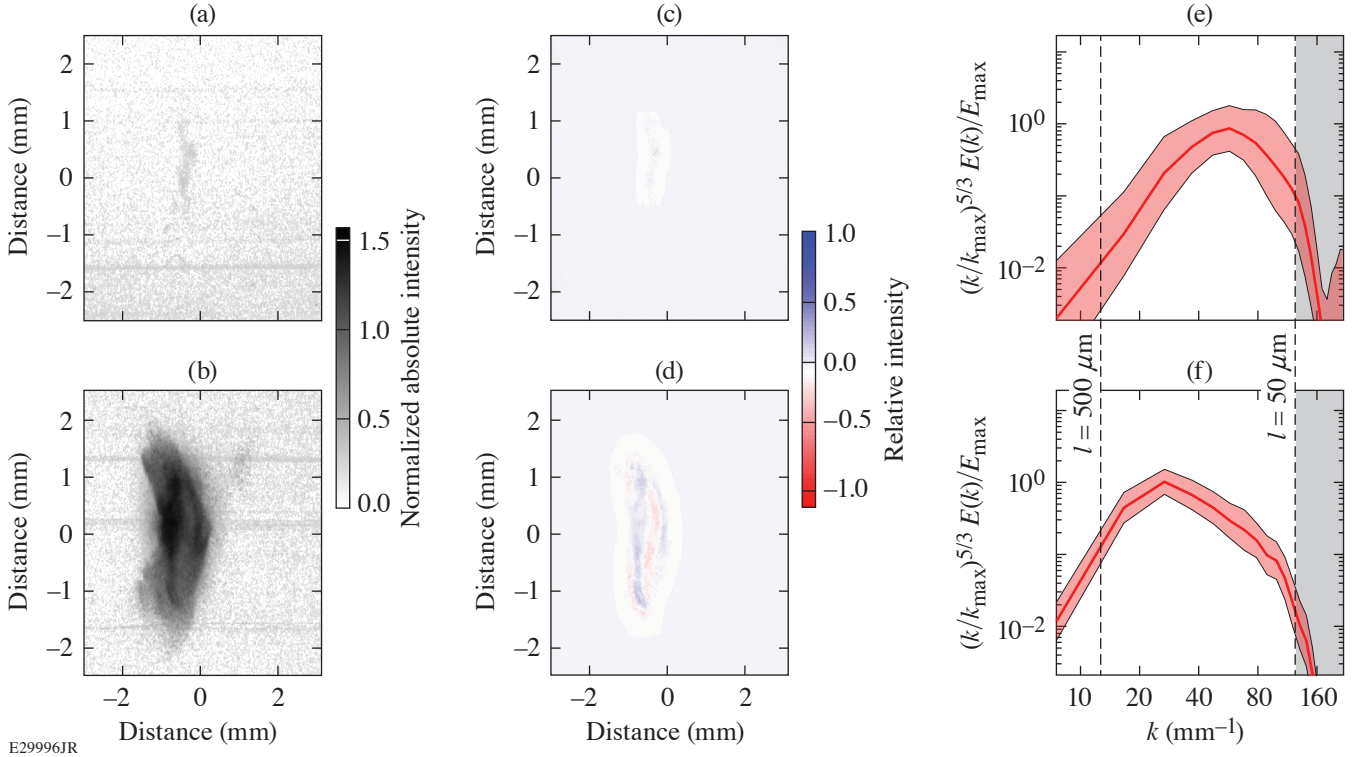

Figure 28

Experimental results. (a) X-ray image of the turbulent interaction region from the 2× magnification framing camera, without the heater beams, at 32.5 ns. (b) Same as (a) but with the heater beams turned on. (c) Relative intensity showing the fluctuations in the turbulent plasma. (d) Same as (c) but with the heater beams turned on. (e) Preliminary power spectra of the turbulent kinetic energy for the two cases in (c) and (d), normalized by the peak energy and boosted by $k^{-5/3}$ (i.e., Kolmogorov scaling) to better display the viscous cutoff. (f) Same as (e) but with the heater beams turned on.

with Los Alamos National Laboratory, Subcontract B632670 with LLNL, and grants No. DE-NA0002724, DE-NA0003605, and DE-NA0003934 to the University of Chicago, DE-NA0003868 to the Massachusetts Institute of Technology, and Cooperative Agreement DE-NA0003856 to the Laboratory for Laser Energetics, University of Rochester. We acknowledge support from the U.S. DOE Office of Science Fusion Energy Sciences under grant No. DE-SC0016566 and the National Science Foundation under grants No. PHY-1619573, PHY-2033925, and AST-1908551. Awards of computer time were provided by the U.S. DOE ASCR Leadership Computing Challenge (ALCC) program, using resources at ANL, which is supported by the U.S. DOE Office of Science under contract No. DE-AC02-06CH11357. We acknowledge funding from grants 2016R1A5A1013277 and 2017R1A2A1A05071429 of the National Research Foundation of Korea. Support from AWE plc., the Engineering and Physical Sciences Research Council EP/M022331/1, EP/N014472/1, and EP/R034737/1, and the U.K. Science and Technology Facilities Council is also acknowledged.

Implementation of a Monochromatic Talbot–Lau X-Ray Deflectometer for Electron Density Diagnostics in High-Energy-Density Physics

Principal Investigators: M. P. Valdivia, D. Stutman, and M. K. Schneider (Johns Hopkins University); V. Bouffetier, G. Perez-Callejo, and A. Casner (Universite de Bordeaux-CNRS-CEA, CELIA)
Co-investigators: C. Stoeckl, C. Mileham, T. Filkins, S. Fess, and M. Romanofsky (LLE)

The proper characterization of the underdense plasma conditions in laser–plasma interactions is key to the study of high-energy-density-physics.[48] Laser–plasma instabilities have been observed to negatively impact hohlraum performance in ICF, for example. These instabilities and their growth depend on the density profile of coronal plasma. Therefore, many experiments performed in large laser facilities, such as LLE, will benefit from accurately measuring electron density profiles in the corona, where the laser–plasma interactions are most active. Moreover, measurements above critical density would help benchmark codes and simulations that currently fail to accurately predict the plasma ablation dynamics of thin foils irradiated by nanosecond pulse lasers. An NLUF experiment proposed the continuation of previous OMEGA EP campaigns that aimed to characterize the ablation front of laser-irradiated foils by mapping x-ray refraction angle and measuring electron density ($\eta_e \approx 10^{23}$ cm^{-3}) through Talbot–Lau x-ray deflectometry (TXD).[49] The latest experiment tested a monochromatic version of the OMEGA EP TXD diagnostic (Fig. 29) developed by Johns Hopkins University under NNSA (HEDLP and NLUF) and LaserNetUS grants.[50]

Copper wire and oil targets were driven by 10-ps laser pulses of 150 to 450 J (~1 to 9 × 10^{17} W/cm^2) to obtain K_α emission. The x-ray backlighting from the targets enabled monochromatic TXD moiré imaging at 8 keV. The diagnostic performance was

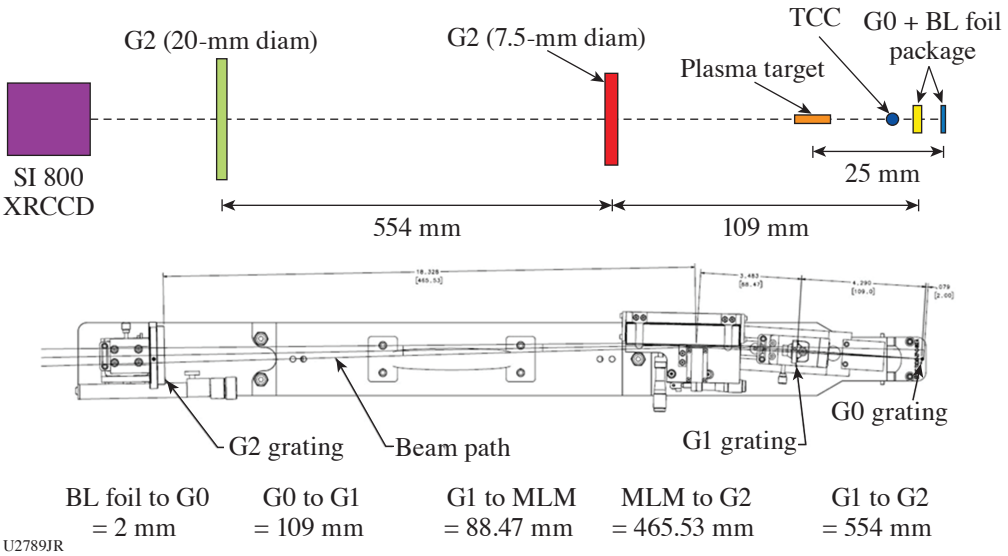

Figure 29
Schematic of the Talbot–Lau interferometer monochromatic configuration (EP-M-TXD) including a multilayer mirror selecting 8-keV x rays.

compromised by the low photon flux measured at the detector surface. In view of these first results, photon flux optimization was prioritized over plasma ablation imaging in this campaign. Moiré images of ~70 counts were acquired by an x-ray CCD (Fig. 30), equivalent to ~50 photons per pixel calculated assuming ~7×10^{-4} conversion efficiency of laser light into Cu K_α photons, CCD with quantum efficiency >50% at 8 keV, interferometer transmission of ~20%, and an attenuation factor of 6 in the blast shield, detector light-blocking filter, and the CH target. Based on previous experiments,[49] at least 300 counts were expected on the CCD surface when considering ~25% mirror reflectivity. From these results, it was concluded that new source grating fabrication methods reduced transmission by a factor of ~3 to 4 (Ref. 50). Foil targets irradiated normally with an additional 5° increased counts on shot 34898 when compared to shot 34889 [Fig. 30(a)]. Moreover, 6.9% contrast was measured for shot 34898 versus 4.7% for shot 34889 [Fig. 30(b)]. The improved fringe contrast may be attributed to the specific source grating used since they are replaced on each shot. When performing *ex-situ* alignment with a Cu anode x-ray tube, measured moiré fringe contrast was higher for the specific rail and source grating used in shot 34898 when compared to shot 34889 (26% versus 19%). Furthermore, moiré fringe contrast and transmission differed for each source grating. Nevertheless, monochromatic TXD diagnostic procedures for *ex-situ* multilayer mirror and grating alignment were successful. The demonstration of reference moiré image acquisition through phase stepping is an important campaign outcome since it will allow for accurate attenuation, phase, and scatter retrieval through TXD methods not requiring an additional laser shot to obtain a reference image.[51]

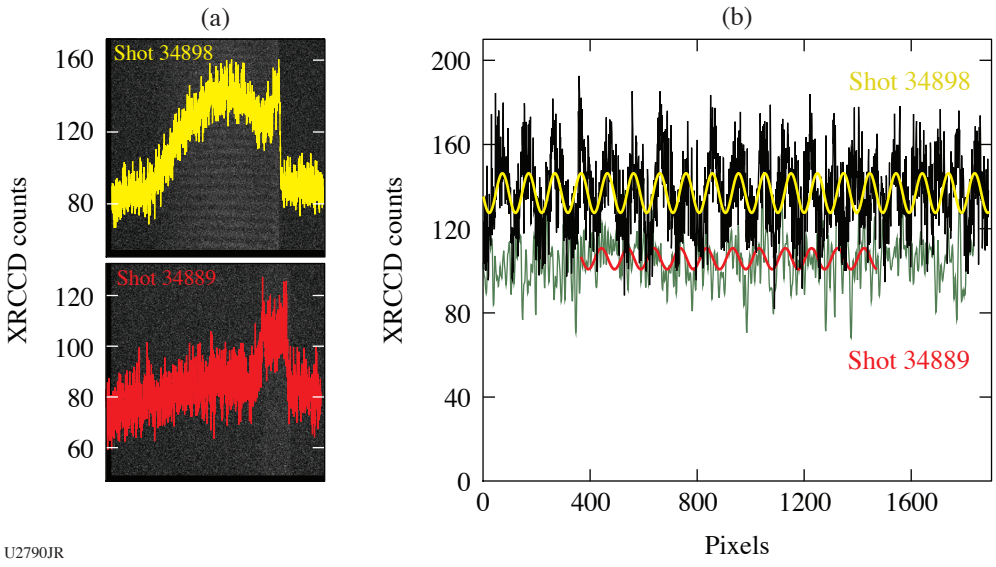

Figure 30
(a) Monochromatic TXD experimental moiré images from the NLUF (FY21) Campaign. X-ray backlighting was provided by irradiating Cu foils at ~150 J, 11 ps, 72-μm spot size for shots 34898 and 34889. Shot 34889 shows a 200-μm Ta slab placed in the middle of the image; no object is present for shot 34898. (b) Moiré fringe profiles used to measure fringe contrast of ~5% for shot 348989 and ~7% for shot 34898.

Optimal conditions for generating x-ray backlighters suitable for TXD will be pursued in future experiments. Spatial resolution and flux optimization will be performed on the Multi-Terawatt (MTW) laser by varying the laser pulse length and energy as well as Cu backlighter target geometry, using source gratings with higher transmission. Monochromatic x-ray backlighting optimization on MTW will inform an upcoming OMEGA EP experiment with the goal to map electron density from a laser-produced plasma object. Note, a recent Laboratory Basic Science Campaign used standard TXD diagnostics to probe the ablation front of an irradiated CH foil. Moiré fringe shifts were observed and 2-D maps of phase, transmission, and dark field were retrieved using an *ex-situ* reference image obtained through phase-stepping. Therefore, once x-ray backlighter optimization is achieved, higher moiré fringe contrast from the monochromatic TXD diagnostics presented here will enable improved electron density, scatter, and elemental composition diagnostic capabilities for HEDP.

This work was supported by U.S. DOE/NNSA HEDLP: DE-NA0003882 and NLUF: DE-NA0003941.

Electron Exhaust Jet and Kinetic Instabilities in a Magnetic Reconnection Experiment Using Laser-Driven Capacitor Coils

Principal Investigtors: S. Zhang, A. Chien, and H. Ji* (Princeton University); L. Gao (Princeton Plasma Physics Laboratory); E. G. Blackman (Department of Physics and Astronomy, University of Rochester); R. K. Follett, D. H. Froula, and J. Katz (LLE); W. Daughton (LANL); C. K. Li, A. Birkel, and R. D. Petrasso (MIT); and J. Moody and H. Chen (LLNL)
*Also Princeton Plasma Physics Laboratory

Magnetic reconnection is a dramatic conversion of magnetic-field energy to plasma flows and energetic particles via a change of magnetic-field topology. In collisionless plasmas, current-driven instabilities may lead to thermalization and electron–ion coupling, providing a major pathway for dissipation in magnetic reconnection. The development of laser-driven capacitor coils in HEDP experiments has provided an unprecedented avenue to study laboratory plasma magnetic reconnection. Kilojoule lasers can drive 10- to 100-kA current in the coils and generate >100-T magnetic fields, producing magnetic-pressure–dominant plasmas akin to the solar corona or magnetosphere. In this OMEGA experiment, we combined the laser-driven capacitor-coil experiments with time-resolved collective Thomson scattering to study the kinetic physics in the collisionless reconnection, including the evolution of the non-Maxwellian velocity distribution function, electron jets, and the kinetic instabilities.

The experimental platform is shown in Fig. 31. The capacitor-coil target is made of a 50-μm-thick Cu foil. The 600-μm-diam coils have 500-μm-long legs and are separated by 600 μm. The magnetic field generated by the capacitor-coil targets is profiled by proton radiography.[52–54] The upstream magnetic-field strength is ~40 T at 6 ns after the laser's onset. The proton radiography also shows the center feature indicating the reconnection current sheet.

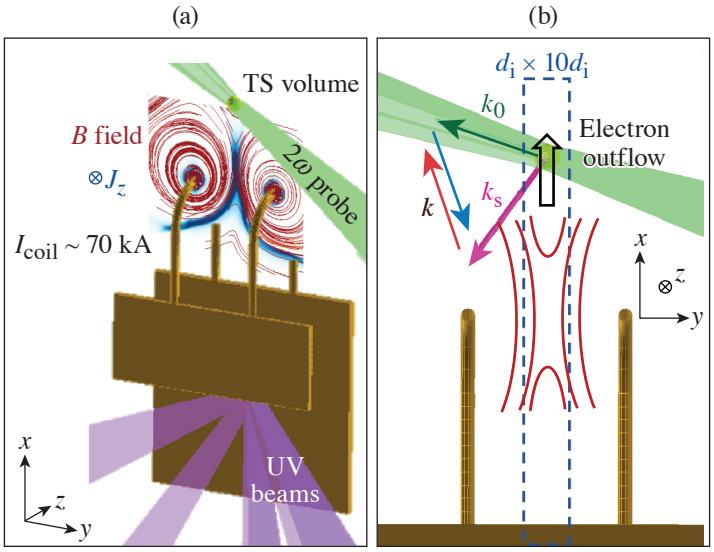

Figure 31
Experimental setup. Six beams of a 500-J, 1-ns UV laser are used to irradiate the back plate of the capacitor, driving current in the coils with I_{coil} ~ 70 kA. *FLASH* MHD simulation results are overlapped in (a) to show the structure of the magnetic field (red lines) and the out-of-plane current density (blue) in the z direction. A 2ω (527 nm) TS beam (green) probes the reconnection exhaust region, 600 μm above the center point between the top of the coils. The k_0 and k_s in (b) are the wave vectors of the probe beam and the collected scattered light. The red and blue arrows indicate wave vectors (k) of waves in plasma that scatter the probe light to the collector. These k's are in the x–y plane and 17° off the outflow direction.

The non-Maxwellian distribution and the kinetic instabilities of the reconnection exhaust are shown in the spectrogram of the Thomson scattering. As shown in Fig. 32(a), the IAW-resonant scattering is bursty and asymmetric. The asymmetric IAW spectrum before the bursts can be reproduced in the synthetic TS spectrum with relative drift between electrons and ions as shown in Fig. 32(c). The bursts confirm the existence of the current-driven ion-acoustic instabilities. Figure 32(b) shows that the asymmetric IAW peaks are accompanied with an electron-acoustic wave (EAW) resonant peak, which needs a two-stream distribution to reproduce as shown in Fig. 32(d).

We acknowledge the Omega Laser Facility staff at the Laboratory for Laser Energetics. This work was performed under the auspices of U.S. DOE NNSA under the AIBS program, and the DOE Office of Science under the HEDLP program with award No. DE-SC0020103.

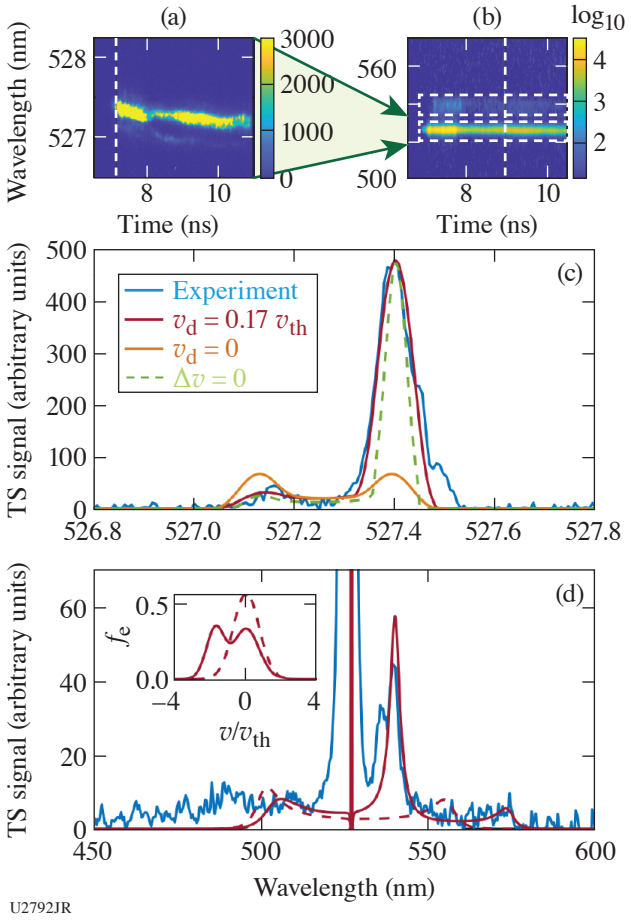

Figure 32
[(a),(b)] Time-resolved TS at t = 7 to 10 ns. The IAW resonant peaks in (a) are highly asymmetric (10:1 to 100:1). (c) The spectrum along the vertical dashed line of (a) before the IAW bursts and the comparison with the synthetic TS spectra. The highly asymmetric IAW's can be reproduced with electrons streaming relative to ions with $v_d \sim 0.17\ v_{th}$. (b) The EAW peak along with the IAW feature. The spectrum at 9 ns [along the vertical dashed line of (b)] is plotted in (d) with a fitted synthetic spectrum (solid red line). A two-stream electron distribution is needed to reproduce the strong EAW signal. The distribution is shown as the solid line in the inserted plot. For reference, the synthetic TS spectrum from a Maxwellian distribution is shown as the dashed line.

1. H. Sio *et al.*, Rev. Sci. Instrum. **87**, 11D701 (2016).
2. N. Kabadi *et al.*, Rev. Sci. Instrum. **92**, 023507 (2021).
3. T. Nagayama *et al.*, Phys. Plasmas **21**, 050702 (2014).
4. D. Kawahito *et al.*, Phil. Trans. R. Soc. A **379**, 20200052 (2021).
5. C. McGuffey *et al.*, Bull. Am. Phys. Soc. **65** (2020).
6. K. Bhutwala *et al.*, "Transport of an Intense Proton Beam from a Cone-Structured Target Through Plastic Foam with Unique Proton Source Modelling," submitted to Physical Review E.
7. C. McGuffey *et al.*, Sci. Rep. **10**, 9415 (2020).
8. C. A. Walsh *et al.*, Plasma Phys. Control. Fusion **64**, 025007 (2022).
9. J. R. Davies *et al.*, Phys. Plasmas **26**, 022706 (2019).
10. A. B. Zylstra *et al.*, Phys. Rev. Lett. **119**, 222701 (2017).

11. B. Lahmann *et al.*, Rev. Sci. Instrum. **92**, 083506 (2021).
12. G. Ren *et al.*, Phys. Rev. Lett. **118**, 165001 (2017).
13. M. Hohenberger *et al.*, Rev. Sci. Instrum. **92**, 033544 (2021).
14. W. Riedel *et al.*, High Energy Density Phys. **37**, 100861 (2020).
15. W. M. Riedel *et al.*, Phys. Plasmas **28**, 122702 (2021).
16. H. G. Rinderknecht *et al.*, Phys. Rev. Lett. **114**, 025001 (2015).
17. H. Sio *et al.*, Phys. Plasmas **26**, 072703 (2019).
18. H. Sio *et al.*, Phys. Rev. Lett. **122**, 035001 (2019).
19. A. Krygier *et al.*, Rev. Sci. Instrum. **89**, 10F114 (2018).
20. Y. P. Opachich *et al.*, Phys. Plasmas **24**, 063301 (2017).
21. P. A. Keiter and R. P. Drake, Rev. Sci. Instrum. **87**, 11E338 (2016).
22. J. J. MacFarlane, J. Quant. Spectrosc. Radiat. Transf. **81**, 287 (2003).
23. L. Gao *et al.*, Astrophys. J. Lett. **873**, L11 (2019).
24. K. D. Meaney *et al.*, Bull. Am. Phys. Soc. **65** (2020).
25. P. M. Nilson *et al.*, Phys. Rev. Lett. **97**, 255001 (2006).
26. M. J. Rosenberg *et al.*, Nat. Commun. **6**, 6190 (2015).
27. A. E. Raymond *et al.*, Phys. Rev. E **98**, 043207 (2018).
28. S. Ivancic, "Channeling Experiments on OMEGA EP," Ph.D. thesis, University of Rochester, 2015.
29. N. L. Kugland *et al.*, Rev. Sci. Instrum. **83**, 101301 (2012).
30. L. Biermann and A. Schlüter, Phys. Rev. **82**, 863 (1951).
31. R. A. Fonseca *et al.*, in *Computational Science – ICCS 2002*, edited by P. M. A. Sloot *et al.*, Lecture Notes in Computer Science, Vol. 2331 (Springer, Berlin, 2002), pp. 342–351.
32. R. G. Hemker, Ph.D thesis, UCLA, 1999.
33. P. T. Campbell *et al.*, Phys. Rev. Lett. **125**, 145001 (2020).
34. D. B. Schaeffer *et al.*, Phys. Rev. Lett. **119**, 025001 (2017).

35. D. B. Schaeffer *et al.*, Phys. Rev. Lett. **122**, 245001 (2019).

36. S. Malko *et al.*, Appl. Opt. **61**, C133 (2022).

37. M. G. Haines, Phys. Rev. Lett. **78**, 254 (1997).

38. A. V. Arefiev *et al.*, Phys. Plasmas **23**, 056704 (2016).

39. A. E. Hussein *et al.*, New J. Phys. **23**, 023031 (2021).

40. E. N. Parker, *Cosmical Magnetic Fields: Their Origin and Their Activity*, The International Series of Monographs on Physics (Clarendon Press, Oxford, 1979).

41. R. M. Kulsrud *et al.*, Astrophys. J. **480**, 481 (1997).

42. A. Brandenburg and Å. Nordlund, Rep. Prog. Phys. **74**, 046901 (2011).

43. P. Tzeferacos *et al.*, Phys. Plasmas **24**, 041404 (2017).

44. P. Tzeferacos *et al.*, Nat. Commun. **9**, 591 (2018).

45. A. F. A. Bott *et al.*, Proc. Natl. Acad. Sci. **118**, e2015729118 (2021).

46. B. Fryxell *et al.*, Astrophys. J. Suppl. Ser. **131**, 273 (2000).

47. P. Tzeferacos *et al.*, High Energy Density Phys. **17**, 24 (2015).

48. R. Paul Drake, *Introduction to High-Energy-Density Physics*, High-Energy-Density Physics: Foundation of Inertial Fusion and Experimental Astrophysics, edited by R. P. Drake (Springer International Publishing, Cham, 2018), pp. 1–20.

49. M. P. Valdivia *et al.*, Rev. Sci. Instrum. **87**, 11D501 (2016).

50. M. P. Valdivia *et al.*, Rev. Sci. Instrum. **91**, 023511 (2020).

51. M. P. Valdivia *et al.*, Appl. Opt. **57**, 138 (2018).

52. L. Gao *et al.*, Phys. Plasmas **23**, 043106 (2016).

53. A. Chien *et al.*, Phys. Plasmas **26**, 062113 (2019).

54. A. Chien *et al.*, Phys. Plasmas **28**, 052105 (2021).